Intelligent operation monitoring and finite element coupled identification of hyperstatic structures

Zhiwu Zhou [a,*] , Zhifeng Zhao [b], Julián Alcalá [c], Víctor Yepes [c]

[a] *Hunan Provincial Key Laboratory of Intelligent Protection and Utilization Technology in Masonry Artifacts, Hunan University of Science and Engineering, Yongzhou Hunan 425006, China*
[b] *Guizhou University of Engineering Science, Bijie Guizhou 551700, China*
[c] *Institute of Concrete Science and Technology (ICITECH), Universitat Politècnica de València, València 46022, Spain*

ABSTRACT

The safety, longevity, and healthy operation and maintenance of world-class large bridges are a research hotspot that continues to attract attention from academia and industry. In particular, during the sustainable operation period of large and statically indeterminate bridges under various loads and complex environmental conditions, it is necessary to establish an information-based intelligent structural health monitoring and early warning cloud platform system to ensure the safety and economic efficiency of in-service bridges. Through interdisciplinary research in computer science, communication engineering, automation control, and engineering mechanics, this article established a multi-factor complex modal multi-source theoretical model and applied the real-time early warning of bridge monitoring data and the coupling of finite element models to verify the robustness of the intelligent cloud model under the influence of multiple factors on statically indeterminate bridges. This work solves the technical barriers that traditional technical monitoring cannot achieve continuous real-time, spatio-temporal and remote monitoring of statically indeterminate structures, and realizes an intelligent cloud platform model for spatial, direct and automated monitoring, providing scientific and technological guarantees for the healthy maintenance of super-large bridges, and providing theoretical scientific support and paradigms for saving labour and reducing maintenance costs.

1. Introduction

The structural dynamic response and fatigue damage of existing long-span bridges, under normal operations and multi-load interactions, are the factors which cause bridge failure. Microscopic cracks inside the structure gradually propagate into macroscopic cracks under repetitive loading, until the structure undergoes instability, fracturing, cumulative fatigue damage and then failure [1]. The fatigue failure of reinforced concrete structures comprises three aspects: steel bar fatigue [2]; concrete fatigue [3]; and fatigue failure at the bonding interface between the steel bars and the concrete [4]. In response to these failure mechanisms, researchers have introduced models which consider critical damage degree, linear cumulative damage theory, machine learning, Monte Carlo cross-validation, fatigue life assessment, and damage-fracture mechanics, in order to study the lifespan of bridges [5, 6].

A comprehensive analysis of the various failure mechanisms in structures aims to explore targeted preventive measures, in order to reduce the risk of failure and the damage caused in the structural field. Regular inspection and monitoring are essential for assessing the health of structures. Continuous monitoring can detect any early warning signs before a problem becomes a major incident; it can identify, inspect, and maintain hidden dangers in a timely manner [7]. In the early days, trained inspectors inspected superficial defects and damage, such as fatigue cracks, visually but this method is inaccurate and prone to errors. In order to improve accuracy and prevent catastrophic failures, structural health monitoring has attracted the attention of researchers because of its low cost and continuous, reliable, and accurate monitoring. However, the integration of energy-saving wireless sensor platforms, to achieve long-term autonomous monitoring, is challenging due to the lack of suitable sensors. There is a lack of effective algorithms for predicting and diagnosing local fatigue damage [8]. In recent years, unlimited intelligent sensors for structural monitoring have received much attention, Such as the wireless sensor network design of Mica-Z

motes [9]. The use of the wireless intelligent sensor framework proposed by iMote2 and the Xnode sensor trigger sensing platform [10] have achieved robust, efficient, and effective monitoring. One disadvantage is that point-type and distributed one-dimensional sensors are difficult to monitor under extreme strain requirements because of their small size limitations and limited ductility [11]. In structural health monitoring, there are two main algorithms: model-based methods and data-driven methods. The former uses an accurate finite element model, which is a time-consuming method [12]. The latter monitors and analyses continuous time series data, transmits wireless networks with low data transmission rates, and extracts and compresses data through high-performance sensor nodes [13]. This work takes the advantages of these two methods and combines them with innovative high-efficiency algorithms to advancing research into continuous health monitoring.

For extra-large bridge projects, it is necessary to take effective measures, such as health monitoring, early warnings, and status assessments during their normal service life, to control structural damage and predict potential hazards [14]. Advanced health monitoring systems can be used to realise data analysis and processing, structural health diagnosis, and intelligent monitoring, to ensure the safety, durability, and normal functioning of bridges over their operational lifespan [15]. Researchers have implemented a dynamic, continuous, real-time online structural safety monitoring model by using electronic, spatial orientation, automation, and remote communication technologies, combined with big IoT data. Structural health monitoring systems mainly consist of three stages: data acquisition (sensing, regulation, and processing), data communication and storage, and health assessment (the implementation of data diagnosis algorithms and information management) [16]. A health monitoring system for a bridge comprises:

- Monitoring of the surrounding environment of the bridge to determine environmental loads.
- Monitoring of the operational loading of the bridge to determine any overloading by vehicle traffic, as well as the operational loading model.
- Monitoring of the static and dynamic characteristics of the structure.
- Monitoring of the static and dynamic responses of the structure to determine the geometric deformation, stress distribution, fatigue state, and cable forces of the structure.

Yong Binbin et al. [17] developed a 3D visualisation system, which realised functions regarding model importing, 3D displays, free rotation and scaling, multi-angle sectioning, real-time monitoring point observations, the display of calculation results, and deformation effect simulations, etc. Yuan Luo et al. [18] investigated the probability of fatigue damage in pre-stressed concrete bridges under random traffic loads and corrosive conditions, simulating the fatigue stress state by establishing a three-stage traffic growth model.

Traditional stress spectrum monitoring and analysis methods are selected according to the design specifications or finite element simulation, which cannot truly reflect the load excitation response of the structure during its service life. Rather, it only collects and accumulates a large amount of environmental excitation information and structural monitoring responses through the original health monitoring sensing equipment over a long time period, realising the data source analysis of the fatigue stress spectrum [19]. Al-Ali et al. [13–20] proposed an IoT-based intelligent road and bridge health monitoring and early warning system, which strengthened the safety and management control of existing bridges through a low-cost autonomous monitoring system. The intelligent health monitoring system, combined with digital twin technology, is used to collect more accurate data through a cloud platform by using video-based digital models based on image scanning. In particular, the configuration of innovative and advanced fibre Bragg grating sensors can achieve a highly sensitive integrated early warning information system for bridges [21].

Based on established road and bridge health monitoring and the

early warning systems and published research in this field (Fig. 2), studies have mainly focused on the exploration of stiffness loss during short-term (temporary field observation) assessments of bridge health status and the influence of temperature-related structural deformations over different time intervals, as well as fatigue, corrosion, erosion, vibration, and other factors. At present, advanced methods and monitoring technologies are seldom used for carrying out long-term, effective, and continuous intelligent early warning monitoring work [22]. This is particularly true for statically indeterminate large-span structures because of their complexity, interference from uncertain influencing factors, and long-term fatigue damage in natural environments. It is even more necessary to explore the problem of structural fatigue damage under the interaction of multiple factors by combining the measured data of the long-term intelligent health monitoring system with the coupling optimisation of the multi-scale finite element model [23] (Fig. 2).

The innovation points of this article are (Fig. 1):

- The analysis is completed by using multiple interdisciplinary cross-studies regarding computer science, communication engineering, automation control, engineering mechanics, and economics. Establishing complex multi-factor and multi-source modal theory: used to analyze the impact of multiple factors on statically determinate bridge structures, and to complete early warning monitoring on the intelligent cloud platform, providing a paradigm for structural safety monitoring during the operation of the existing floating system.
- IoT-based real-time automated online monitoring is adopted for the bridge, which solves the problem that traditional technology monitoring cannot, achieving continuous spatiotemporal monitoring and large-scale and long-distance monitoring of the structures. Our study realises the transformation of infrastructure health monitoring from a "point-based, indirect, curve-fitting" to a "spatial, direct, continuous monitoring" mode, through the comprehensive functions of automatic collection, transmission, processing and analysis of monitoring data and automatic early warnings, providing a technical guarantee for intelligent health operations.
- This article provides an effective control and early warning system model for multiple damage behaviour such ascracking, deformation, aging, damage, and the dynamic vibration of statically indeterminate structures. We clearly present the feasibility of the structure, in terms of integrity, safety, durability, and strength controllability, providing a theoretical basis and case study data for the long-term maintenance and warranty of complex structures.

The article is divided into five sections: Section 1 introduces the current status and shortcomings of research in this field through a literature review; Section 2 describes the theoretical model and research methods; Section 3 presents the advanced intelligent monitoring and finite element coupling analysis of statically indeterminate structures; Section 4 discusses the monitoring data anomalies and the comparative coupling optimisation of the established finite element model; and Section 5 summarises the innovation points and scientific contributions of this article to the field, including a discussion of the shortcomings of this article.

2. Methodology

The theoretical model and intelligent monitoring system described in this article is divided into seven sections. In the intelligent monitoring system, the algorithm developed through the cloud platform continues to automate data recognition and optimise capture (Fig. 3).

2.1. Structural fatigue damage

Under repetitive loading, microscopic cracks gradually propagate into macroscopic cracks until the crack propagation becomes unstable.
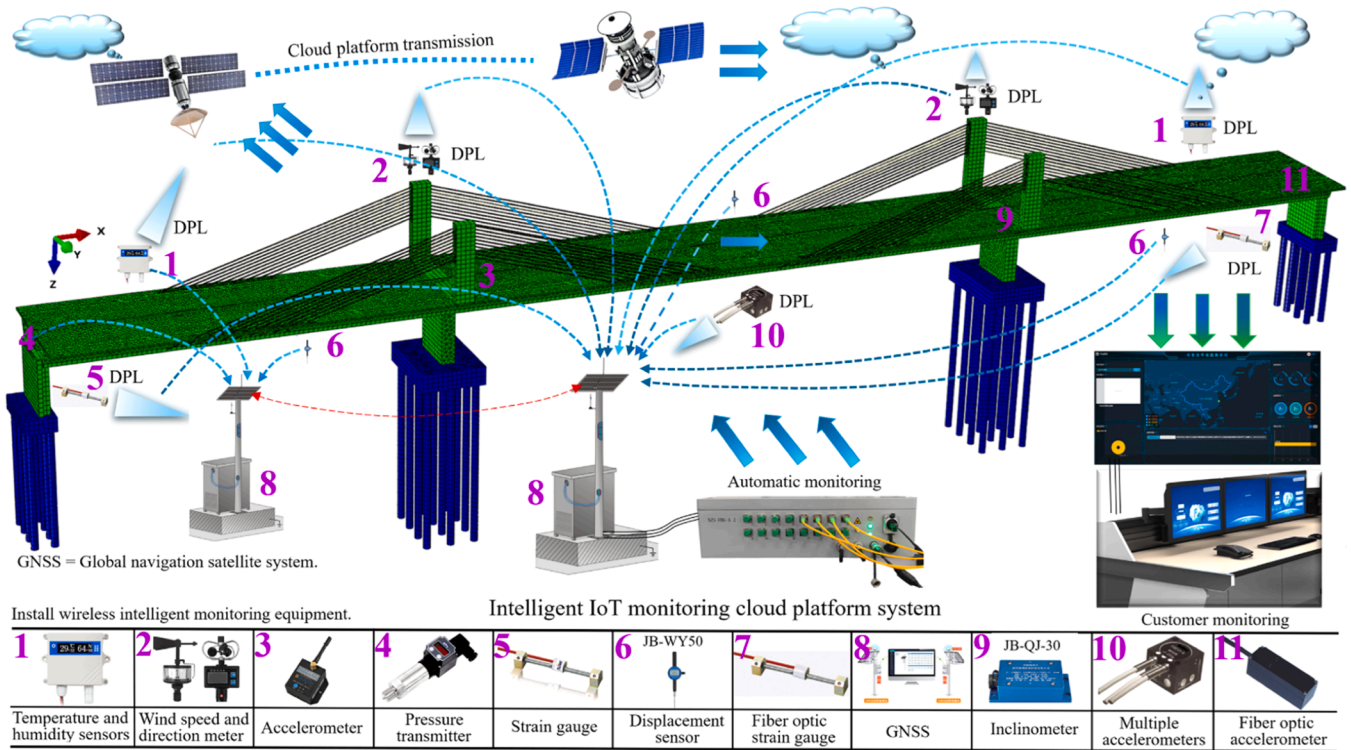
Fig. 1. Intelligent bridge health monitoring system.
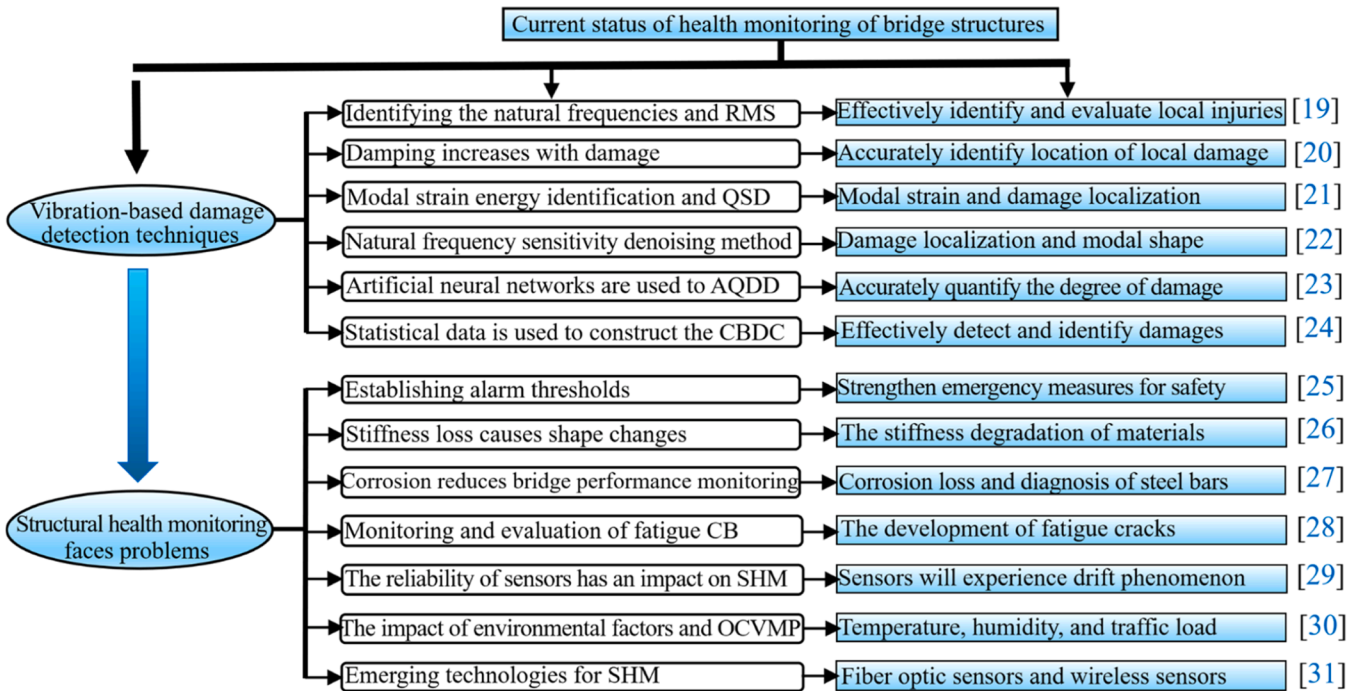
CB = Cracks in bridges; SHM = Structural health monitoring; RMS = Resonant modes of the structure; OSD = Quantification of structural damage; AQDD = Accurately quantify degree of damage; CBDC = Correlation between damage characteristics; OCVMP = Operating conditions on vibration monitoring performance.

Fig. 2. Investigation and analysis of the current research status and existing problems in this field [19–31].

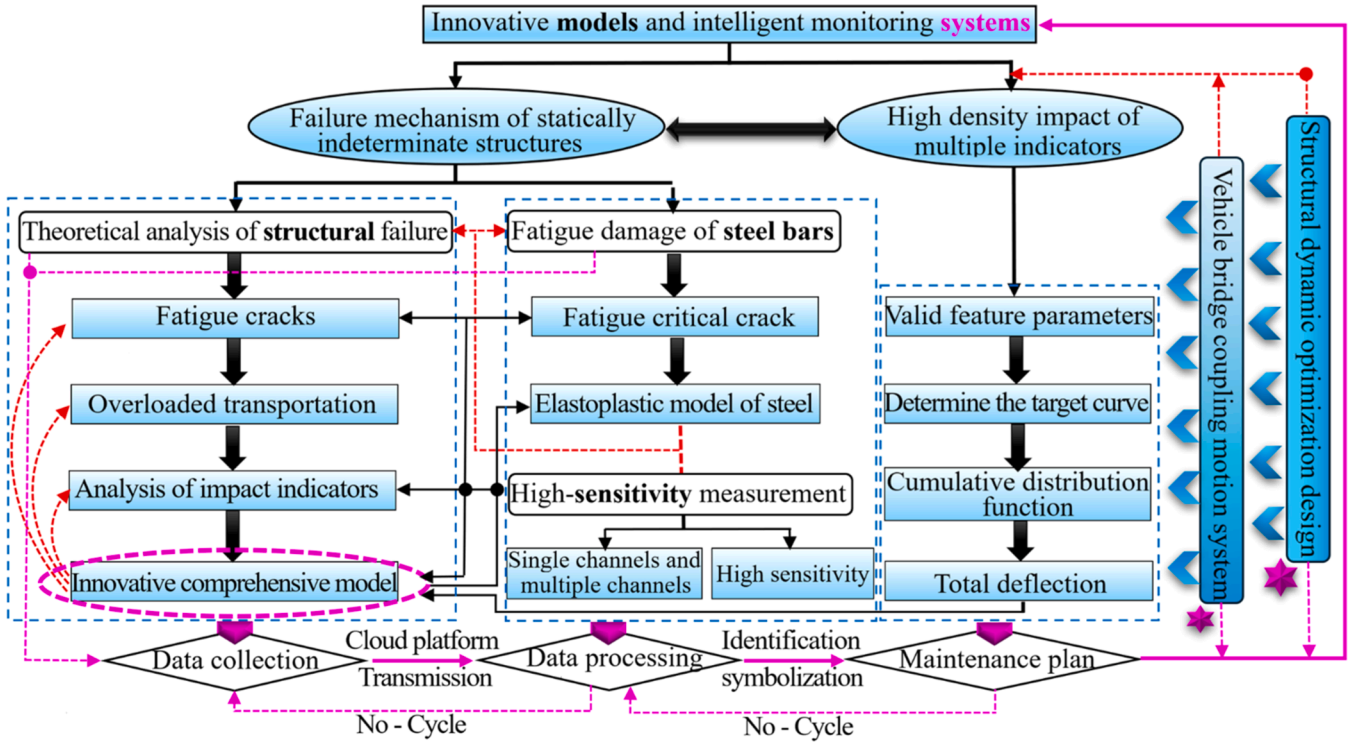**Fig. 3.** The theoretical model and intelligent monitoring systems of this article demonstrating innovation and relevance.

The nonlinear cumulative fatigue damage model of a structure is [24]:

$$D = 1 - \left\{ 1 - \frac{(\alpha+1)N_{b1}}{B(\beta+3)} \times \sum_{i=1}^{m_{rb}} [(\alpha_{ai} + 2\sigma_{mi}) \times \sigma_{ai}]^{\frac{\beta+3}{2}} \right\}^{\frac{1}{(\alpha+1)}} \quad (1)$$

Where D is the damage index; B, α and β are material constants; N_{b1} is the current number of block cycles; i is the number of cycles; σ_{ai} is the stress amplitude; and α_{mi} is the average stress of the ith cycle (Pa).

During the calculation of the cumulative fatigue damage of structures under the influence of overloaded traffic, it is necessary to consider the proportion of overloaded vehicles (by axle-weight and gross-weight) in the vehicle traffic, as shown in Eq. (2) [32]:

$$D_{cum}(t) = N_{avg} \times t \times \left(r_{AL} \times \sum_i^t \frac{n_i \times S_i^m}{A} + r_{GW} \times \sum_j^t \frac{n_j \times S_j^m}{A} \right) \quad (2)$$

Where N_{avg} is the average annual truck traffic on the bridge (vehicles/year); t is the service time (year); r_{AL} and r_{GW} are the proportion of axle-weight overloaded trucks in overloaded vehicle traffic and the proportion of gross-weight overloaded vehicles (%); n_i and n_j are the number of stress cycles generated; and S_i and S_j are the bridge stress amplitudes caused by axle-weight and gross-weight overloaded vehicles (Pa).

The bridge fatigue damage function is:

$$g(X) = D_{crit} - N_{avg} \times t \times \left(r_{AL} \times \sum_i^t \frac{n_i \times S_i^m}{A} + r_{gw} \times \sum_j^t \frac{n_j \times S_j^m}{A} \right) \quad (3)$$

Where $g(X) < 0$ is the probability of fatigue failure; m is the slope of the S - N curve; A is the fatigue constant; and D_{crit} is the critical fatigue damage.

Research has shown that, when the number of fatigue loading cycles increases, the modulus of elasticity of concrete continuously degrades, and the calculation of the residual fatigue strain is [33,34]:

$$\Delta\varepsilon_r(N) = \Delta\varepsilon_r(1) + \frac{k_1 \times \varepsilon_{max}^{k_2} \times (1 - \varepsilon_{min}/\varepsilon_{max})^{k_3}}{\varepsilon_k^{k_5}} N^{k_4} \quad (4)$$

Where $\Delta\varepsilon_r(N)$ is the residual fatigue strain after N cycles of fatigue loads k_1, k_2, k_3, k_4, and k_5; ε_{max} and ε_{min} are the initial instantaneous strains under the upper and lower fatigue load limits; and ε_k is the coefficient of the residual strain in the concrete, developed to the third stage (i.e. a rapid decrease of the modulus of elasticity until fatigue failure).

Assuming that there are n groups of statically indeterminate structural components, the residual strain is: $\varepsilon_Z = \sum_{i=1}^n \Delta\varepsilon_r(N)$. The component satisfies the damage model and elastic-plastic model under the influence of uncertain factors by adopting the incremental constitutive theory. The three-dimensional component has a tension zone, compression zone and tension-compression zone, which generate compression and tension stresses of σ_1 and σ_2, respectively, and satisfy $\sigma_n = E_r \times (\varepsilon - \varepsilon_r)$.

$$\left\{ \begin{matrix} \sigma_1 \\ \sigma_2 \end{matrix} \right\} = \begin{bmatrix} (1-d_t) & 0 \\ 0 & (1-d_c) \end{bmatrix} \times \left\{ \begin{matrix} \sigma_1' \\ \sigma_2' \end{matrix} \right\} \quad (5)$$

Where d_t is the tensile damage parameter of the structural component; d_c is the compressive damage parameter of the structural component; σ_1' is the derivative of the tensile zone parameter; σ_2' is the derivative of the compressive zone parameter; 1 represents the tensile stress; 2 represents the compressive stress; and $\varepsilon_{t,r}$ is the tensile strength and represents the tensile stress and strain corresponding to $f_{t,r}$.

$$\sigma_1 = E_{r1} \times (\varepsilon_1 - \varepsilon_Z) \rightarrow \sum_{i=1}^n \sigma_i = \sum_{i=1}^n [E_{ri} \times (\varepsilon_i - \varepsilon_Z)]$$

and so

$$\sum_{i=1}^n \sigma_i = \sum_{i=1}^n \left[E_{ri} \times \left(\varepsilon_i - \sum_{i=1}^n \Delta\varepsilon_r(N) \right) \right].$$

Combining the analytical model with Eq. (5) yields:

$$\left\{\begin{array}{c} \sum_{i=1}^{n} \sigma_{i1} \\ \sum_{i=1}^{n} \sigma_{i2} \end{array}\right\} = \begin{bmatrix} (1-d_{t1}) & 0 \\ 0 & 1-d_{c2} \end{bmatrix}$$

$$\times \left\{\begin{array}{c} \sum_{i=1}^{n} \sigma_{i1}' = \sum_{i=1}^{n} \left[E_{ri1} \times \left(\varepsilon_{i1} - \sum_{i=1}^{n} \Delta\varepsilon_r(N)\right)\right]' \\ \sum_{i=1}^{n} \sigma_{i2}' = \sum_{i=1}^{n} \left[E_{ri2} \times \left(\varepsilon_{i2} - \sum_{i=1}^{n} \Delta\varepsilon_r(N)\right)\right]' \end{array}\right\} \quad (6)$$

$$d_t = 1 - \rho_t \left[1.2 - 0.2\left(\frac{\varepsilon}{\varepsilon_{t,r}}\right)^5\right], \varepsilon_{t,r} \in \left(\varepsilon_{t,r}^{min} \to \varepsilon_{t,r}^{max}\right) \quad (7)$$

$$Soweget: \left\{\begin{array}{c} \sum_{i=1}^{n} \sigma_{i1} \\ \sum_{i=1}^{n} \sigma_{i2} \end{array}\right\} = \begin{bmatrix} \left(1 - \left\{1 - \rho_{t1}\left[1.2 - 0.2\left(\frac{\varepsilon}{\varepsilon_{t1,r}}\right)^5\right]\right\}\right) & 0 \\ 0 & 1 - \left\{1 - \rho_{t2}\left[1.2 - 0.2\left(\frac{\varepsilon}{\varepsilon_{t2,r}}\right)^5\right]\right\} \end{bmatrix} \times$$

$$\left\{\begin{array}{c} \sum_{i=1}^{n} \sigma_{i1}' = \sum_{i=1}^{n} \left[E_{ri1} \times \left(\varepsilon_{i1} - \sum_{i=1}^{n} \Delta\varepsilon_r(N)\right)\right]' \\ \sum_{i=1}^{n} \sigma_{i2}' = \sum_{i=1}^{n} \left[E_{ri2} \times \left(\varepsilon_{i2} - \sum_{i=1}^{n} \Delta\varepsilon_r(N)\right)\right]' \end{array}\right\} \quad (8)$$

Eq. (8) is a data model for the limit derivative of the internal structural energy of a three-dimensional component under the effects of multiple factors. The hyperstatic structure is based on a nonlinear failure model. The state function of the structure is constructed to obtain the failure probability, and the obtained structural failure probability is used as a nonlinear structural reliability evaluation indicator. The parameter identification results of the nonlinear probability model are used as random variable inputs. A proxy model of the influences and responses of multiple uncertain factors can be constructed to analyse the theoretical hyperstatic structural model: $D_t^i = f\left(\left\{\begin{array}{c} \sum_{i=1}^{n} \sigma_{i1} \\ \sum_{i=1}^{n} \sigma_{i2} \end{array}\right\}\right) d\left(\left\{\begin{array}{c} \sigma_{i1} \\ \sigma_{i2} \end{array}\right\}\right).$

The established model is based on the limit interval $\left(\varepsilon_{t,r}^{min} \to \varepsilon_{t,r}^{max}\right)$, so $\lim_{t\cup i \to n} \left\{f\left(\left\{\begin{array}{c} \sum_{i=1}^{n} \sigma_{i1} \\ \sum_{i=1}^{n} \sigma_{i2} \end{array}\right\}\right) d\left(\left\{\begin{array}{c} \sigma_{i1} \\ \sigma_{i2} \end{array}\right\}\right)\right\} \in \left(\varepsilon_{t,r}^{min} \to \varepsilon_{t,r}^{max}\right)$. At this point, the analysis of the mathematical model is complete, and the abbreviated equation can be shown as Eq. (9).

The geometric nonlinear analysis of statically indeterminate structures should consider the triggering factors.

The multi-factor complex modal multi-source theoretical model ($D \to D_{cum}(t) \to g(X) \to \Delta\varepsilon_r(N)$):

$$f'(D_t^i) = \lim_{t\,\cup\,i \to \infty} D_{cum} \frac{f(minN_{avg}) - f(maxD_{crit})}{S_i - S_j} \in [\varepsilon_{min} \to \varepsilon_{max}] \quad (9)$$

2.2. Steel fatigue damage

Experimental studies have shown that the fatigue life of reinforced concrete bridges is mainly determined by the fatigue of the steel bars, and the life of the bridge is determined by the fatigue fracture of the main load-bearing steel bars under multiple random amplitude stresses.

The critical crack depth of the fatigue failure of a steel bar is given by [35]:

$$a_{fr} = min\left\{\frac{1}{\pi}\left(\frac{K_{ic}}{\gamma\sigma_{max}}\right)^2, a_y\right\} \quad (10)$$

Where a_{fr} is the critical crack depth of steel bars (mm); k_{ic} is the fracture toughness of the material; γ is the geometric correction coefficient for calculating the stress intensity factor, which is determined by the radius r of the steel bar and the crack depth a; and a_y is the crack depth of the steel bar at yield (mm).

Based on the ideal elastoplastic model of steel bars, it can be assumed that the fatigue stiffness of steel bars does not degrade. Combined with the S - N double logarithmic curve of steel bars, the constitutive model of steel bars after multiple fatigue loads is obtained as [36]:

$$\sigma(N) = \begin{cases} E_s\varepsilon(N) & \Delta\varepsilon_r(N-1) < \varepsilon(N) \leq \varepsilon_y(N) \\ f_y(N) & \varepsilon(N) > \varepsilon_y(N) \end{cases} \quad (11)$$

Where $\sigma(N)$ is the residual stress of the steel bar after N times of fatigue loads (Pa); E_s is the initial modulus of elasticity of the steel bar; f_y is the initial yield strength of the steel bar; and $\varepsilon_y(N)$ and $\Delta\varepsilon_r(N)$ are the yield strain and residual strain of the steel bar after N times of fatigue loading, respectively.

Fibre optic sensors are sensors that measure displacement based on grating Moiré patterns and they can achieve highly sensitive measurements of single channels and multiple channels. Their configuration depends on the bandwidth of the light source and the dynamic range of the measurement parameters; it is necessary to consider the demodulation limit of the fibre grating demodulator and the actual strain of the measured object. Assuming that the sensor needs to measure n sets of grating points, the wavelength variation of all grating points on the fibre grating string channel is calculated by [37,38]:

$$\begin{cases} \Delta\lambda = \Delta\lambda_1 + \Delta\lambda_2 + \Delta\lambda_3 + \cdots\cdots + \Delta\lambda_n = \sum(K_\varepsilon \times \varepsilon) \\ \lambda_n = \Delta\lambda = \sum(K_\varepsilon \times \varepsilon + \lambda) \leq \lambda_{max} \end{cases} \quad (12)$$

Where $\Delta\lambda$ is the range of wavelength variation for calculating a single grating; ε is the strain value of the nth grating point; K_ε is the strain sensitivity of the nth grating point. λ_n is the measurement range of n sensors; and λ_{max} is the maximum measurement range for a single channel of the fibre grating demodulator.

2.3. Multi-load effect characteristics

The monitoring data of multiple indicators of bridges are affected by different sequences and the accurate identification and extraction of valid feature parameters are prerequisites for statistical analysis. Multiple single-peak distribution features are used to determine the target

curve function through various fitting methods and then the curve integral is normalised; the cumulative distribution function is calculated to obtain a Gaussian mixture model of multi-peak probability density features [39], which is then used to verify the matching and accuracy of the parameters.

$$f(x) = \sum_{i=1}^{k} \varphi_i \frac{1}{\sqrt{2\pi}\sigma_i} \exp\left(-\frac{(x-\mu_i)^2}{2\sigma_i^2}\right) \tag{13}$$

Where $f(x)$ is the Gaussian mixture model; k is the order of the Gaussian mixture model; and φ_i, μ_i and σ_i are the combined weights, mean, and standard deviation of the ith order function.

The deflection of a bridge consists of the deflection caused by the live load, temperature stress, pre-stress loss, concrete shrinkage and creep, with a total deflection of [40]:

$$f = \varepsilon_L \times f_L + \frac{\left(f_t^* - \mu_f\right)}{\sigma_f} + \varepsilon_V \times f_V \tag{14}$$

Where f_L is the deflection live load effect; f_T is the deflection temperature effect; f_V is the long-term deflection; ε_L and ε_V are residual identification coefficients for live load deflection and long-term deflection; f_t^* is the original temperature induced deflection; μ_f is the mean of the temperature induced deflection; and σ_f is the standard deviation of the temperature induced deflection.

2.4. Vehicle bridge coupling

Bridges generate mutual mechanical effects under their loads and external loads, whilst vehicles exert gravity, damping, and inertia forces on the bridges. The equation for a coupled motion system is constructed by establishing the displacement coordination and force balance conditions between vehicles and bridges [41]:

$$\begin{cases} M_b\ddot{u}_b + C_b\dot{u}_b + K_bu_b = F_bM_v\ddot{u}_v + C_v\dot{u}_v + K_vu_v = F_vM_{bv}(t)\ddot{\delta} + C_{bv}(t)\dot{\delta} \\ +K_{bv}(t)\delta = F_{bv}(t) \end{cases} \tag{15}$$

Where M_b and M_V are the mass matrices of bridges and vehicles; C_b and C_V are the damping matrices of bridges and vehicles; K_b and K_v are the stiffness matrices of bridges and vehicles; $\ddot{u}$, $\dot{u}$ and u are column vectors of acceleration, velocity, and displacement; F_b and F_v are the vehicle-to-bridge mutual forces; $M_{bv}(t)$ is the generalised mass matrix of the vehicle-bridge coupling system; $C_{bv}(t)$ is the damping matrix of the system; $K_{bv}(t)$ is the stiffness matrix of the system; δ is a column vector, composed of the various degrees of freedom and generalised modal coordinates of the vehicle; and $F_{bv}(t)$ is the generalised load column vector of the system.

2.5. Structural dynamic optimisation

During the structural dynamic optimisation design, it is necessary to carry out multiple analyses of structural dynamic characteristics and
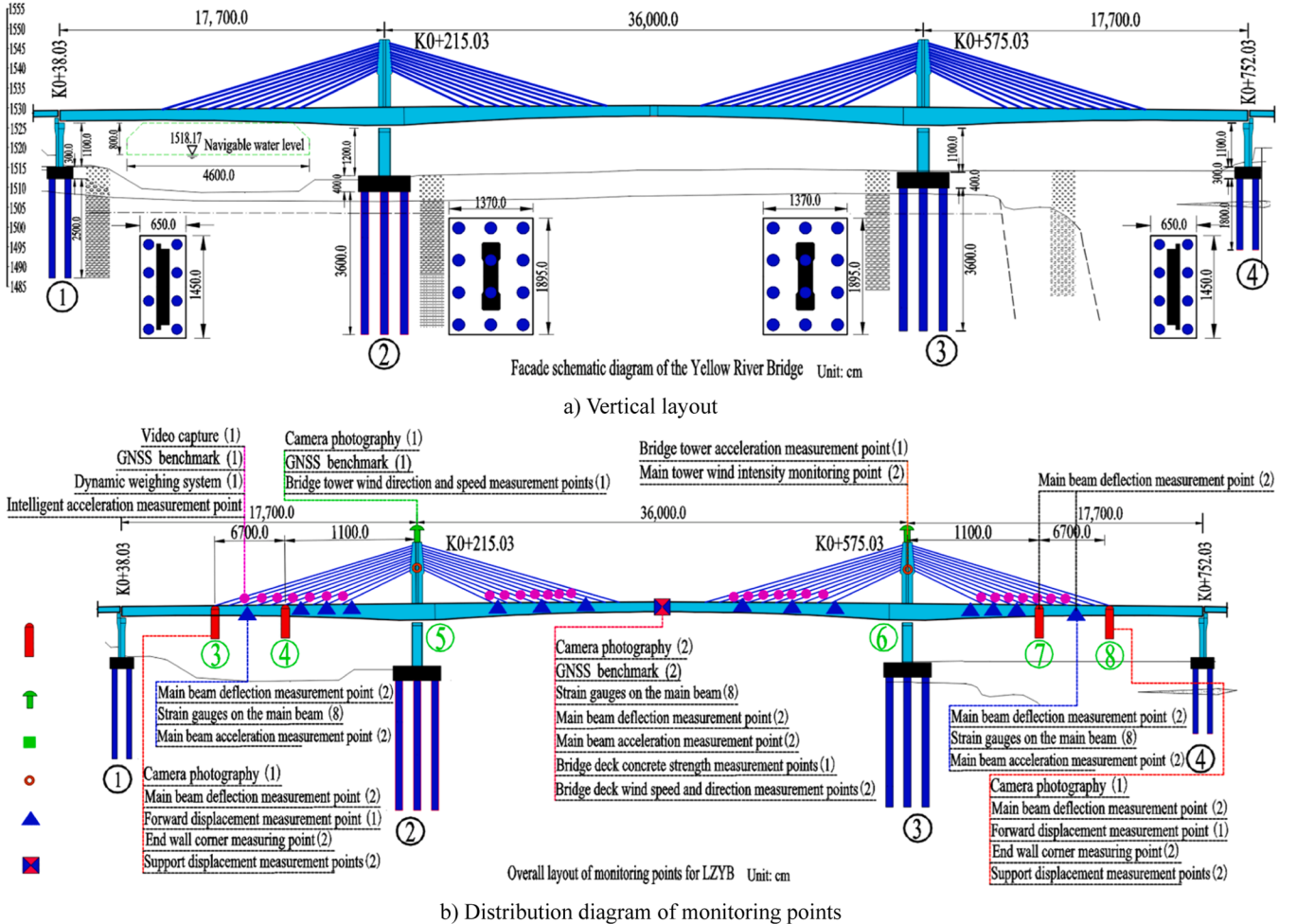

Facade schematic diagram of the Yellow River Bridge   Unit: cm

a) Vertical layout

b) Distribution diagram of monitoring points

Fig. 4. Diagram of LZYB.

dynamic responses. The dynamic optimisation criteria method has the advantages of fewer re-analyses and a faster convergence rate. The mathematical model for structural dynamic optimisation design is constructed as a Lagrangian function and then the design variable A_n is derived on both sides of the function; the design variable adjustment factor $S_1 (0 < S_1 < 1)$ is introduced to construct the design variable after the nth iterative optimisation [35].

$$\begin{cases} A'_n = f_n A_n \ \left(A_n^l < f_n A_n < A_n^u\right) \\ f_n = S_1 + \dfrac{1 - S_1}{\partial W(A_n)/\partial A_n} \times \left\{ -\displaystyle\sum_{i=1}^{k} \alpha_i \frac{\partial g_i}{\partial A_n} + \sum_{j=1}^{l} \beta_j \frac{\partial h_j}{\partial A_n} \right\} \end{cases} \quad (16)$$

Where A'_n is the design variable after iterative optimisation; f_n is the iterative correction coefficient for the design variables; A_n is the design variable; A_n^u and A_n^l are the upper and lower limits of the design variables, respectively; W is the objective function with design variables; and α_i, β_i and ξ_n are Lagrange multipliers.

3. Results

The main bridge span of the Yellow River Bridge in China (referred to as LZYB) is a span of 714 (177+360+177) m (Fig. 4), with a 2 × 40 m simply supported box beam (south bank) and a 5 × 40 m continuous box-girder (north bank) as the approach bridges. The bridge tower comprises a reinforced concrete rhombic tower, with a transverse width of 450 cm and a longitudinal width of 700 cm for the upper tower column section, as well as a transverse width of about 4.5-9.0 m and a longitudinal width of 7.0-10.0 m for the lower tower column section. A box-shaped monolithic section, transitioning to a box-shaped partition.

Each bridge tower is equipped with 24 end-bearing cast-in-place piles, with a diameter of 2.5 m and a length of 40 m. The main beam is an I-shaped concrete composite beam, with heights of 2.83 m (at the centre of the main beam) and 3.06 m (at the centre of the bridge). The tower columns are made of C50 concrete, with a height of 151 m (84+67 m) at the south tower and 147 m (84+63 m) at the north tower.

The bridge tower is formed by variable-section double columns, with the tower column adopting a single-box and single-compartment box section. The stay cable is made of galvanised parallel steel wire bundles, with a diameter of 7 mm and a maximum cable length of 187.068 m (cable weight is 17 t).

The standard spacing of the stay cables is 12.0 m and five sizes (PES7-139, 151, 199, 241, and 301) have been used. The bridge design standards are: four-lane expressway extra-large bridge; highway-Class I vehicle load; seismic peak ground acceleration of 0.2 g; design vehicle speed of 80 km/h; design basic wind speed of 10-minute average maximum speed of 25.8 m/s; bridge deck width of 27.5 m (24.5+1.5+1.5 m).

3.1. Monitoring data

The health monitoring of the LZHB was carried out during the through-operation phase, with a focus on structural weaknesses and traffic safety, based on data analysis requirements and the structural

Table 1
Optimised layout of monitoring points and early warning assessment indicators.

Number	Monitoring items	Sensor type	Quantity	Installation location
Environment	Surrounding the environment of the bridge	Temperature and humidity sensor	1	Main beam L/2 section
	Internal temperature of bridge tower		4	Bridge tower cable anchorage zone
Applied load	Vehicle load and traffic volume	Dynamic weighing	4	Stable roadbed location
	Wind speed on bridge deck and tower top	Wind speed and direction meter	4	Three bridge decks; One each at the top of the tower
	Structural temperature	Strain gauge	72	Installation of strain gauges
	Bridge shore surface site	Accelerometer	1	Downstream stable roadbed
	The top of the pier or the bottom of the pier		4	5 # and 6 # bridge piers
Structural response	Vertical displacement of the main beam	Pressure transmitter	48	Main bridge structural components
	Lateral displacement of the main beam	GNSS	3	Bridge L/2, upstream and downstream bridge decks
	Displacement of supports and beam ends	Displacement meter	10	Position of support and beam joints
	Tower top offset	GNSS	2	Two bridge tower tops
	Horizontal and vertical corners of beam ends	Inclinometer	4	Beam end, crossbeam
	Key sections of main beams and cable towers	Fiber Bragg Grating Strain Gauge	82	Location of bridge towers and cable towers
	Vertical and horizontal vibration acceleration of the main beam	Accelerometer	31	Main beam side span, mid span, and tower
	Cable vibration acceleration	Fiber Bragg Grating Accelerometer	56	Cable arrangement
Number	Monitoring indicators	Warning indicators	Acquisition method	
1	Vehicle model analysis	Identification of rated load (Number of axles; Vehicle length)	Video surveillance	
2	Traffic flow analysis	Four lane expressway (ADT ranges from 2500 to 55000 vehicles)	Video surveillance; Video capture	
3	Overweight analysis	49 tons as the limit (82.5; 110 tons)	Dynamic weighing monitoring	
4	Overspeed analysis	80km/h as the limit	Overspeed flow monitoring	
5	Environmental temperature monitoring	-2 ~ 34.3°C; 9.6 ~ 26.5°C; Control interval:-15 ~ 39°C.	Temperature fiber optic sensor	
6	Environmental humidity monitoring	6.5% ~ 98%; 14.6% ~ 72.7% (Main tower); Prevent corrosion	Humidity fiber optic sensor	
7	Wind load monitoring	0 ~ 18.56m/s; Wind speed < 25.8m/s	Anemometer	
8	Seismic load monitoring	$E_1 < 0.20g$	Ground motion measuring instrument	
9	Structural response monitoring	The natural frequency is lower than the theoretical calculation value	Fiber optic monitoring equipment	

characteristics of the bridge (Fig. 4a). The aim was to promptly identify abnormal information from within the bridge structures, issue timely alarms for direct risk factors, promptly maintain and manage indirect and potential risk factors, and eliminate hazards and hidden dangers. The monitoring consisted of four parts: environmental monitoring, action monitoring, structural response monitoring, and structural change monitoring (Table 1).

The LZYB is shown in Fig. 4b, and it was equipped with ten types of monitoring instruments, totalling 374 devices, installed at the maximum bending moment and shear force positions of the bridge members, based on the principles of design mechanics and structural finite element models. Through the analysis of the characteristics of mechanical inversion in the actual environment of the bridge structure, the mechanical indicator parameters in the intelligent online monitoring environment were compared, forming a health status diagnosis and early warning function. In order to monitor using the IoT-based cloud platform, multi-performance indicator automation was adopted; real-time monitoring data was quickly, efficiently, and accurately transmitted to the monitoring platform via IoT and cloud networks. The data analyses and early warnings were synchronised, avoiding extreme environmental interference.

3.1.1. Characteristics of load strain effects on transportation vehicles

According to the pre-processing results, the analysis of traffic monitoring data using the intelligent monitoring cloud platform, and exporting the recorded data from April to July (an actual operation of five months) from a benchmark database management system, it can be seen that the focus of vehicle load monitoring is to track vehicle weight and trajectory information, including total vehicle weight, axle load, and spatiotemporal motion data.

N_{m4} the total traffic is (total traffic in April) = 100,267 vehicles < N_{m5} = 226,890 vehicles < N_{m6} = 306,066 vehicles < N_{m7} = 418,508

vehicles; the average monthly growth rate is 1: 2.26: 1.35: 1.37; N_{md4} the average daily traffic is N_{md4} (average daily traffic in April) = 10,027 vehicles > N_{md5} = 7,319 vehicles < N_{md6} = 10,202 vehicles < N_{md7} = 14,431 vehicles; the peak period is June and July (Fig. 5a). N_{tov4} (total overweight vehicles in April) = 316 vehicles < N_{md5} = 1,749 vehicles < N_{md6} = 1,872 vehicles < N_{tov7} = 17,711 vehicles; G_{max4}(maximum vehicle weight in April) = 93.0 t (= 32 vehicles (G_w > 49 t as overweight)) < G_{max5} = 93.0 t (G_{dov5} = 56 vehicles) < G_{max6} = 99.3 t (G_{dov5} = 203 vehicles) > G_{max7} = 98.6 t (G_{dov7} = 611 vehicles) (Fig. 5b); N_{sv4} (vehicles exceeding the speed limit in April) = 16,995 vehicles < N_{sv5} = 37,921 vehicles < N_{sv6} = 56,157 vehicles < N_{sv7} = 84,497 vehicles, N_{mvs4} (maximum vehicle speed in April) = 168 km/h (D_{dsv} = 1,700 vehicles) < N_{mvs5} = 198 km/h (D_{dsv} = 1,223 vehicles) < N_{mvs6} = 196 km/h (D_{dsv} = 1,872 vehicles) < N_{mvs7} = 199 km/h (D_{dsv} = 2,914 vehicles) (Fig. 5c).

Three parameters (maximum daily traffic, daily overweight vehicles, and traffic travelling at speeds less than 80 km/h) were selected, to analyse the pattern of changes in monitoring data and polynomial trend fitting curves. Eqs. (12) and (13) were established to obtain R^2_N = 0.560,9, R^2_D = 0.550,3, and R^2_G = 0.654,7, respectively, and to determine the best fitting requirements.

The Complex Plot function algorithm was used to plot the image of the complex variable function, in order to analyse its degeneracy and singularity. The colours correspond to the radius of the complex plane function value, the colours and lines of the three variables gradually widening with the changes in the absolute value of the function. Transparency and colour represent the changes in the modulus and radius of the dependent variable (Figs. 5d, 5e and 5f).

As vehicle load causes high-frequency components to strain, wireless vibrating wire strain gauges were used to monitor and collect the frequency. After the frequency was obtained, the data were directly converted into the equation or the program and then read and transmitted
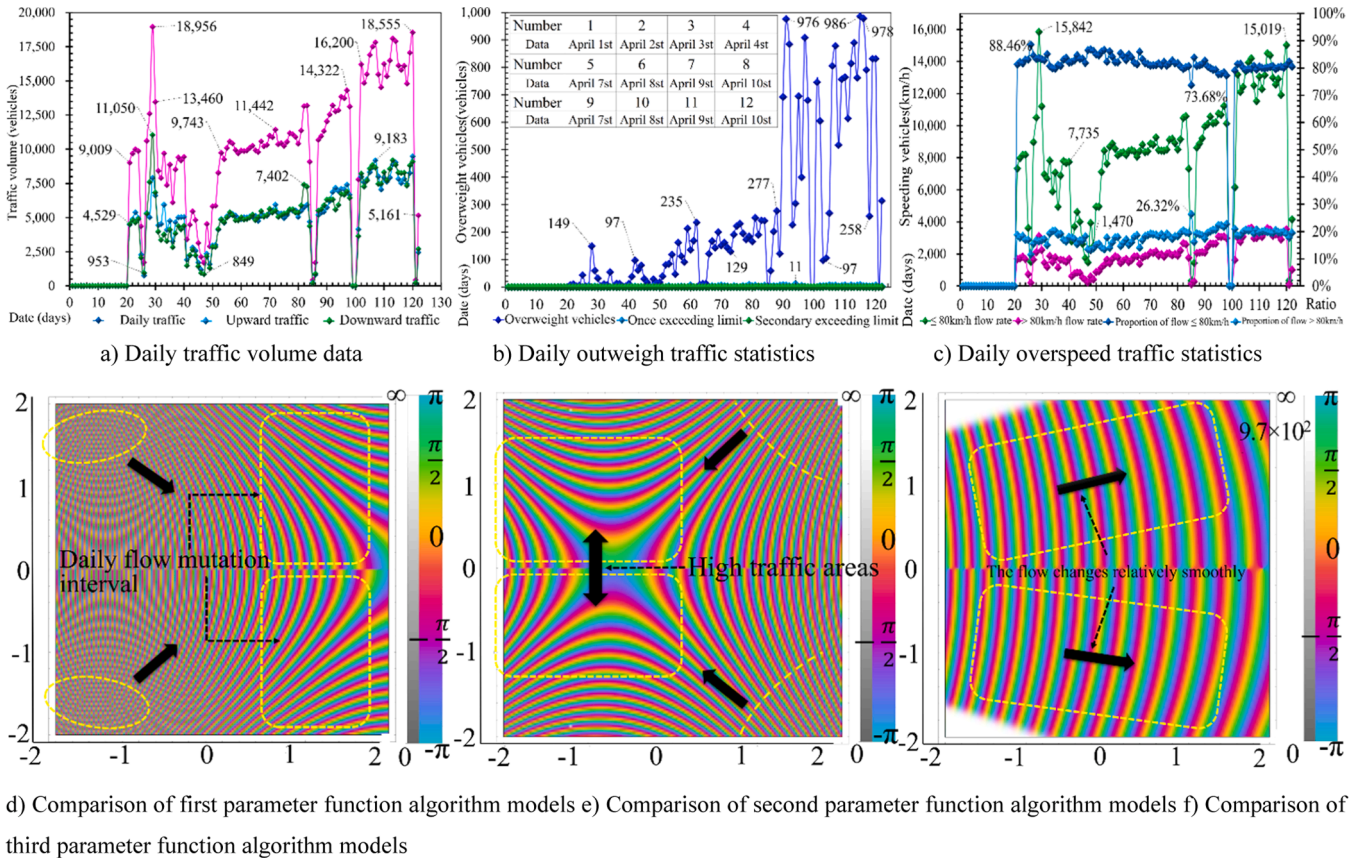

a) Daily traffic volume data b) Daily outweigh traffic statistics c) Daily overspeed traffic statistics

d) Comparison of first parameter function algorithm models e) Comparison of second parameter function algorithm models f) Comparison of third parameter function algorithm models

Fig. 5. Statistical comparison of traffic monitoring data.

to the 4 G vibrating wire acquisition instrument through transmission integration (Fig. 1). Due to the dispersion and uncertainty of overloaded vehicles at different time intervals, non-stationary vehicles had non-stationary strain segments. Strain response eigenvalues (amplitude and maximum) showed obvious multi-peak distribution characteristics but the cumulative data exhibited the multi-peak probability density characteristics of multiple single Gaussian distribution combinations [42].

There were 80 sets of strain monitoring points (Fig. 4). The maximum value interval range was $S_{G03-68-06} = 613.1\mu\varepsilon$ (4.75 spans on the west side, on the inner side of the lower edge of the longitudinal beam) $> S_{G01-48-07} = 603.9\mu\varepsilon$ (2.50 spans on the east side, on the inner side of the lower edge of the longitudinal beam) $> S_{G02-48-06} = 574.2\mu\varepsilon$ (3.50 spans on the west side, on the inner side of the lower edge of the longitudinal beam) $> S_{G04-48-06} = 564.0\mu\varepsilon$ (5.50 span on the west side, on the inner side of the lower edge of the longitudinal beam) $> S_{G03-28-07} = 544.1\mu\varepsilon$ (4.25 spans on the east side, on the inner side of the lower edge of the longitudinal beam) and the minimum value interval range was $S_{G02-48-07} = -225.5\mu\varepsilon$ (3.50 spans on the east side, on the inner side of the lower edge of the longitudinal beam) $> S_{G04-48-08} = -226.2\mu\varepsilon$ (5.50 span on the east side, on the outer side of the lower edge of the longitudinal beam) $> S_{G03-28-05} = -243.9\mu\varepsilon$ (4.25 span on the west side, on the outer side of the lower edge of the longitudinal beam) $> S_{G03-28-06} = -265.0\mu\varepsilon$ (4.25 spans on the west side, on the inner side of the lower edge of the longitudinal beam) $> S_{G03-48-05} = -301.1\mu\varepsilon$ (4.5 span on the west side, on the outer side of the lower edge of the longitudinal beam) (Fig. 7b).

The Gaussian mixture model in Eq. (13) was used to analyse seven parameters: N_{mi}, N_{mdi}, N_{tovi}, G_{maxi}, N_{svi}, N_{mvsi}, and S_{Gi-i-i}. The objective function curve equation was obtained by separately fitting three polynomial combinations. Normalising these equations determined the characteristics of the probability function density, obtaining $R^2_{mi-tovi-svi} = 0.9711$, $R^2_{mi-tovi-Gi} = 0.0825$, $R^2_{tovi-svi-Gi} = 0.0597$, $R^2_{mi-tovi-G} = 0.2094$, $R^2_{mi-svi-G} = 0.1757$, and $R^2_{tovi-svi-G} = 0.1683$. Fig. 8 shows the fitting curve of the probability density function. Based on the feature points of the maximum and minimum values of the function and the clustering characteristics of the data, it was determined that Fig. 8a meets the requirements for the intelligent recognition of non-stationary strain segments but the disadvantage is that the analysis model does not provide feedback on the correlation between on-board and monitoring strain under operating conditions. The goodness of fit of Figs. 8c and 8d are

both $R^2 < 0.500$, and the monitoring data and strain show a discrete distribution in the monitoring time domain.

The established $R^2_{mi-tovi-svi}$ met the fitting requirements and was normalised, based on the polynomial fit, to obtain $f(x,y) = 1,953.2 + 965.595,2 \times x + 123.248,3 \times y - 0.828,4 \times y^2 - 35.908,3 \times x^3 + 34.973,3 \times x^2 \times y - 85.402,1 \times x \times y^2 + 8.473,8 \times y^3 (429 < x < 189,56; 2 < y < 976)$, which is the theoretical calculation of traffic vehicles on LZYB (Figs. 7a and 7c).

According to the fitting analysis of the monitoring data (Figs. 8a and 8b), the structural response of the bridge under discrete vehicle loads is concentrated in the range 3.50~5.50 L on the west side. It is preliminarily concluded that the deflection generated by the bridge structure in this area is a concentrated peak. As the bridge has a reinforced concrete structure, the deflection monitoring can invert the stress state and stiffness change in the bridge structure, which is affected by temperature. Given this, it is necessary to establish a correlation model of monitoring data for the correlation between temperature and deflection and form a correlation model between the vehicles, temperature, and deflection, which is a difficult research problem in the health monitoring of bridges that have super-static determinacy structures [43].

3.1.2. Monitoring deflection temperature effect coupling

Seven temperature and humidity sensors were installed in the LZYB, as shown in Fig. 6 (marked with red circles), which adopted a wireless signal transmission system at a temperature measurement range of -40 to 80 °C and a humidity range of 0-100 °CRH. Forty-two sets of deflection monitoring points were arranged on seventeen sections of the main beam (marked with orange flat circles in Fig. 6), with a monitoring range of 5~500 m. Monitoring and statistical analysis were conducted on the ambient temperature and internal temperature of the bridge tower in the bridge site area from April to July, showing that the ambient temperature in the bridge site area was 36.3 °C $> T > 2$ °C, with a maximum temperature difference of 34.3 °C. The ambient temperature inside the bridge tower was 26.5 °C $> T > 9.6$ °C, with a maximum temperature difference of 16.5 °C. The ambient humidity in the bridge site area and the humidity monitoring data inside the bridge tower were as follows: the ambient temperature in the bridge site area was 98% $> RH > 6.5$%, with a maximum temperature difference of 91.5 °C; the ambient temperature inside the bridge tower was 72.7% $> RH > 14.6$%, with a maximum temperature difference of 56.4 °C (Table 2).

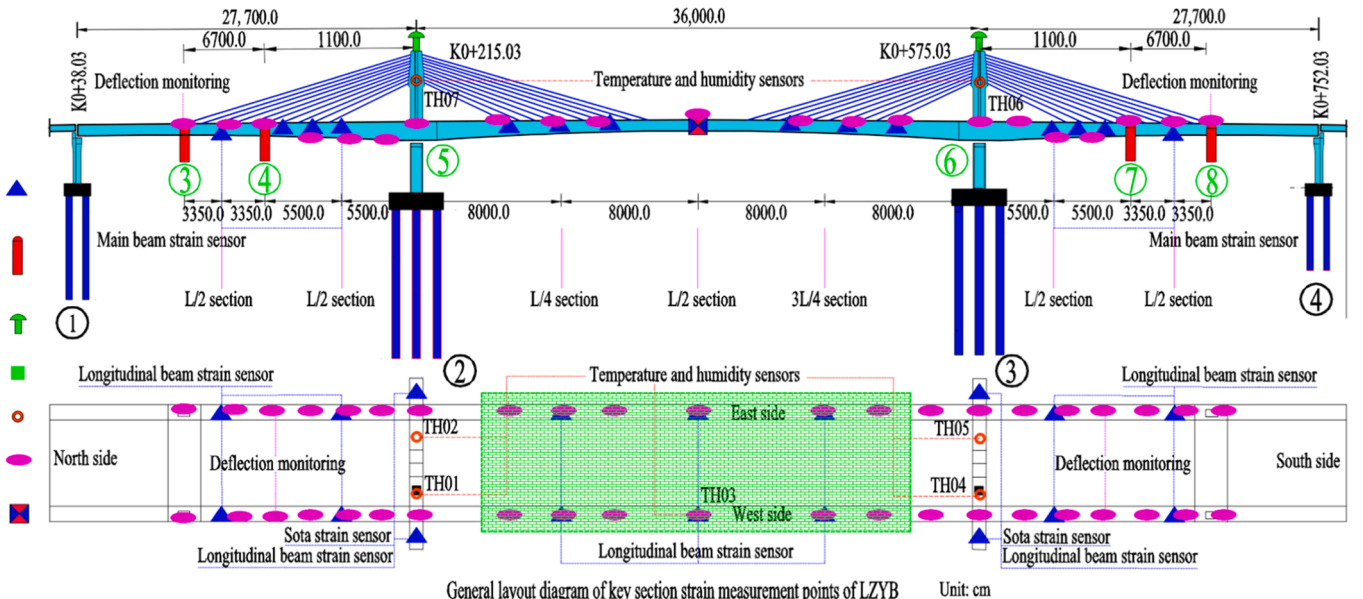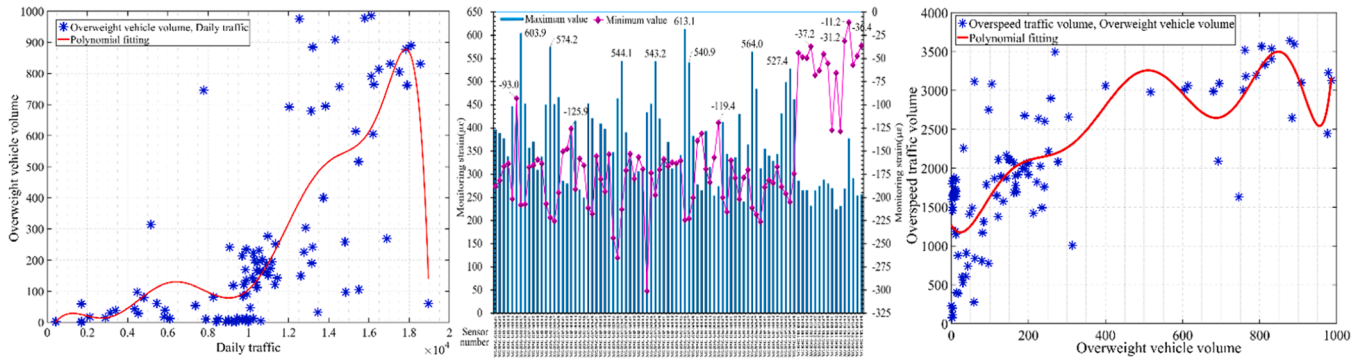The mean of the deflection monitoring was 233.45 mm and there
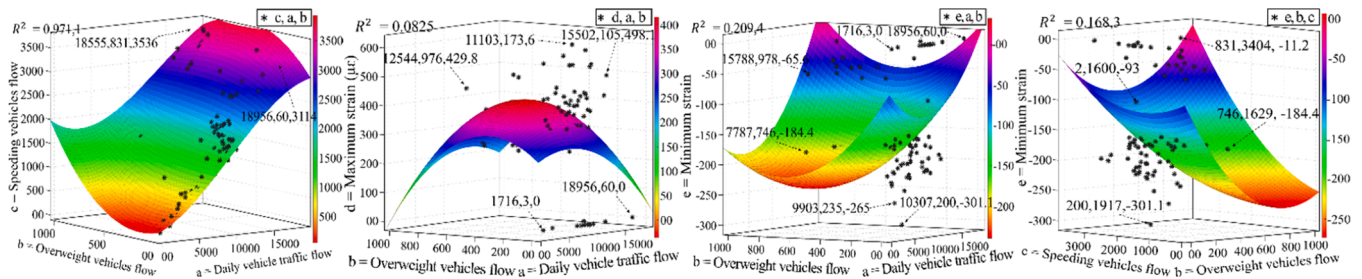

Fig. 6. Schematic diagram of LZYB strain monitoring point layout.

a) Daily traffic volume data b) Daily traffic + overweight vehicle volume c) Overweight vehicle volume + overspeed vehicle volume

Fig. 7. Monitoring data analysis and parameter fitting analysis.

a) Daily traffic + overweight vehicle volume + Speeding vehicles b) Daily traffic + overweight vehicle volume + maximum strain c) Daily traffic + overweight vehicle volume + Minimum strain d) Overweight vehicle volume + Speeding vehicles + Minimum strain

Fig. 8. Probability density function fitting analysis of monitoring parameters.

Table 2
LZYB's environmental temperature, humidity, and deflection monitoring data.

Sensor number	Maximum value (°C)		Minimum value (°C)		Position
	Temperature	Humidity	Temperature	Humidity	
XG-G03-048-01	36.30	98.00	2.00	6.50	4.5 Crossing − East Side
XG-T01-022-01	25.80	66.50	11.10	15.20	4.0 Crossing tower − West Side
XG-T01-022-02	26.40	72.70	11.30	16.30	4.0 Crossing tower − Eastside
XG-T02-022-01	26.50	66.30	10.90	14.60	5.0 Crossing tower − West Side
XG-T02-022-02	26.10	67.30	9.60	16.00	5.0 Crossing tower − Eastside
Sensor number	Number	Sensor number	Number	Sensor number	Number (mm)
XG-G01-008-01	0.00	XG-G03-018-01	12.80	XG-G04-008-01	241.50
XG-G01-008-02	0.00	XG-G03-018-02	13.30	XG-G04-008-02	628.90
XG-G01-048-01	2.10	XG-G03-028-01	20.80	XG-G04-028-01	241.40
XG-G01-048-02	3.20	XG-G03-028-02	469.50	XG-G04-028-02	600.40
XG-G02-008-01	6.80	XG-G03-038-01	26.60	XG-G04-048-01	241.70
XG-G02-008-02	8.20	XG-G03-038-02	510.30	XG-G04-048-02	601.00
XG-G02-028-01	13.50	XG-G03-048-01	31.00	XG-G04-068-01	242.40
XG-G02-028-02	11.40	XG-G03-048-02	558.60	XG-G04-068-02	600.10
XG-G02-048-01	15.00	XG-G03-058-01	101.40	XG-G05-008-01	244.80
XG-G02-048-02	13.60	XG-G03-058-02	556.60	XG-G05-008-02	597.20
XG-G02-068-01	12.90	XG-G03-068-01	107.80	XG-G05-048-01	239.80
XG-G02-068-02	12.50	XG-G03-068-02	571.50	XG-G05-048-02	589.80
XG-G03-008-01	7.80	XG-G03-078-01	195.20	XG-G05-088-01	242.40
XG-G03-008-03	8.80	XG-G03-078-02	607.90	XG-G05-088-02	594.40

were seven sets with $L_d > 200$ mm, in section 4.875L-7.00 L on the west side of the main beam. $L_{XG482} = 628.9$ mm (5.00 pier on the east side) $> L_{XG382} = 607.9$ mm (4.87 pier on the east side) $> L_{XG442} = 601.0$ mm (5.25 pier on the east side) $> L_{XG422} = 600.4$ mm (5.25 pier on the east side) $> L_{XG582} = 597.2$ mm (6.00 pier on the east side). According to the monitoring data time changes, there were relatively large fluctuations, with the temperature, humidity, and deflection values at each monitoring point requiring regression analysis to quantitatively determine their correlation. The corresponding regression parameter values were

calculated using Matlab, as shown in Table 3, with a goodness of fit of $R^2_{d-h} = 0.6333$, $R^2_{d-t} = 0.6953$, $R^2_{h-t} = 0.7152$, all being greater than 0.500, indicating that the model has a good correlation. The data show that the positive correlation between temperature values and deflection values in Fig. 9c is better than those in Figs. 9a and 9b and the root mean square of the regression system is $RMSE_{d-h} = 7.1273 < RMSE_{d-t} = 8.0756 < RMSE_{h-t} = 13.3592$, at its smallest. In conclusion, the analysis is consistent.

Table 3
LZYB's environmental temperature, humidity, and deflection monitoring data.

Model	Regression coefficient	Estimated value	Confidence interval
Polynomial regression fitting	P1	− 4.183,3	− 18.535,8 10.169,3
	P2	−10.503,4	− 24.105,3 3.098,5
	P3	20.142,1	−29.234,7 69.519,0
	P4	25.536,1	−13.877,4 64.949,6
	P5	56.781,7	39.909,3 73.654,2
	$R^2 = 0.633,3$; SSE = 892.338,4; DFE = 5.000; RMSE = 13.359,2		
Polynomial regression fitting	P1	−4.462,7	−13.138,8 4.213,4
	P2	−4.049,7	−12.272,0 4.172,6
	P3	20.854,8	−8.993,3 50.702,9
	P4	9.863,8	−13.961,5 33.689,0
	P5	9.924,0	−0.275,3 20.123,4
	$R^2 = 0.695,3$; SSE = 326.073,5; DFE = 5.000; RMSE = 8.075,6		
Polynomial regression fitting	P1	16.620,1	3.381,4 29.858,8
	P2	−20.064,8	−34.357,4 −5.772,7
	P3	−16.977,6	−37.968,5 4.013,4
	P4	25.448,9	16.851,9 34.045,9
	$R^2 = 0.715,2$; SSE = 304.794,4; DFE = 6.000; RMSE = 7.127,3		

According to the monitoring data and regression model analysis, there were ten sets of monitoring points with a deflection greater than 500 mm, concentrated on the L/8 section to 7L/8 section on the east side of the main beam, with a maximum deflection of 628.90 mm (5.00 L pier on the east side) and a maximum ambient temperature of 36.30 °C (4.50 L pier on the east side).

According to the temperature monitoring data of the structure, the temperature of the longitudinal beam was $48.9 > T > − 3.5$ °C, with a maximum temperature difference of 48.5 °C; the temperature inside the tower T was 28.6 °C $> T > 0$ °C, with a maximum temperature difference of 28 °C. The monitoring data show that the temperature difference causes changes in long-term deflection and interferes with the propagation of signal frequency, so the Waveform Viewer Tool function in the MATLAB signal processing toolbox was used to analyse and visualise the spectral characteristics; the change in internal temperature was displayed through digital filters and variations of signal amplitude with frequency. Fig. 9d shows that the frequency variation range is 10~55 dB, tending to gradually decrease whilst the amplitude remains unchanged.

The internal temperature of the filtered structure was as follows: $T_{XG386} = 48.9$ °C (on the inner side of the lower edge of the longitudinal beam with a 4.5 L span on the west side) $> T_{XG326} = 48.6$ °C (on the inner side of the lower edge of the longitudinal beam with a 4.25 L span on the west side) $> T_{XG366} = 48.5$ °C $> T_{XG586} = 48.5$ °C $> T_{XG246} = 47.9$ °C (on the inner side of the lower edge of the longitudinal beam with a 3.5 L span on the west side).

According to our comprehensive analysis, the area of influence of the temperature on the deflection of LZYB is concentrated at the following positions of the main beams on the west and east sides of ②-③ span (the green area in Fig. 6):

$$\begin{cases} East\ side \quad 4.25L - 4.5L - 5.00L - 5.50L - 6.50 - 7.00L \\ West\ side \quad 4.00L - 4.50L - 4.87L - 5.25L - 5.75L - 6.00L \end{cases}.$$

3.2. Finite element fitting

The modal parameters of bridges include the main geometric and physical quantities, such as vibration frequency, vibration mode, mass, and stiffness, etc. A 3D finite element model was established to correct the bridge structure, with the weights and correction coefficients of the geometric and physical parameters determined through sensitivity parameters. The loading action of LZYB can be divided into four categories, according to the JTGD60-2015 design code: permanent, variable, accidental, and seismic [44–46].

Permanent effects include structural gravity and the buoyancy of water, while variable effects include the lane load, concentrated load, and pressure of the water flow:

- Structural gravity: $G_{k−bridge\ deck} = \gamma \times v_1 = 778.8 \times 25.5 = 19,859.40$ kN; $G_{k−main\ tower} = \gamma \times v_2 = 207.47 \times 26.0 = 53,94.22$ kN; $G_{k−main\ beam} = \gamma \times v_3 = 7,527.90 \times 26.0 = 195,725.40$ kN; $G_{k−lower\ structure} = \gamma \times v_4 = 7,527.90 \times 26.0 = 195,725.40$ kN;
- Buoyancy of water: $F_1 = F_4 = \gamma \times V_1 = 9.8 \times 14.14 = 138.54$ kN; $F_2 = F_3 = \gamma \times V_2 = 9.8 \times 21.21 = 207.82$ kN;
- Lane load: $F_v = q_k \times L = 10.5 \times 300.0 = 3,150.00$ kN;
- Concentrated load: $P_k = 360.00$ kN;
- Pressure of water flow P_k: $F_w = KA \times \gamma v^2/2g = 0.8 \times 7.61 \times 1.50 \times 1.6^2/2 \times 9.81 = 1.19$ kN.

The pedestrian load on the sidewalk slabs, on both sides of the bridge, was taken to be 4.0 kN/m^2, which was calculated as 2,249.55 kN. In terms of accidental action analysis, the value is: 4.0 kN/m^2.

The Yellow River is not navigable at the location of the LZYB and so the impact effect of ships was not considered. The river area is regularly cleared to prevent any floating objects from hitting the bridge and the vehicle impact force for the bridge structure was considered according to a design value of 1,000 kN, with the impact force acting in the area above 1.2 m from the carriageway. In this study, the bridge was monitored during normal operations. It is not located within the seismic zone and so seismic effects were not considered.

The wind loading on the bridge was within the design range. The actual location of the bridge is in a low wind climate zone and so the highest wind force level of 5.7 was considered, this being the strongest recorded wind over the past 70 years.

3.2.1. Finite element coupling analysis

The finite element modelling of LZYB was carried out using Abaqus/CAE 2021 software; 3D, solid shape, and extrusion type models were selected for the modelling space, with an approximate size w of 100.

The bridge mainly comprises C30 and C50 reinforced concrete and steel strands. The relevant parameters are $\rho_{C30} = 2,316$ kg/m^3, $\rho_{C50} = 2,332$ kg/m^3, $\rho_{Steel\ strand} = 7,850$ kg/m^3; the values of modulus of elasticity are $E_{C30} = 28,850$ MP$_a$, $E_{C50} = 33,180$ MP$_a$, and $E_{Steel\ strand} = 206,000$ MP$_a$. Poisson's ratio is $\mu_{C30} = 0.233$, $\mu_{C50} = 0.254$, and $\mu_{Steel\ strand} = 0.300$.

The divided mess sizing controls are one approximate global size, the number of elements is 200,355 sets, and the analysis errors are 0%. The high-quality mess division enhances the scientificity of the finite element coupling analysis.

The finite element coupling of LZYB was completed in 1 s. Figs. 10a and 10b show the three-dimensional Energy, Strain, Stress, and Displacement cloud maps of LZYB, respectively. A total of 115 sets of elements were selected, using tools for MES analysis. The top ten sets of elements in the Energy arrangement were: $E_{42463} = 64,514.75$ J (middle
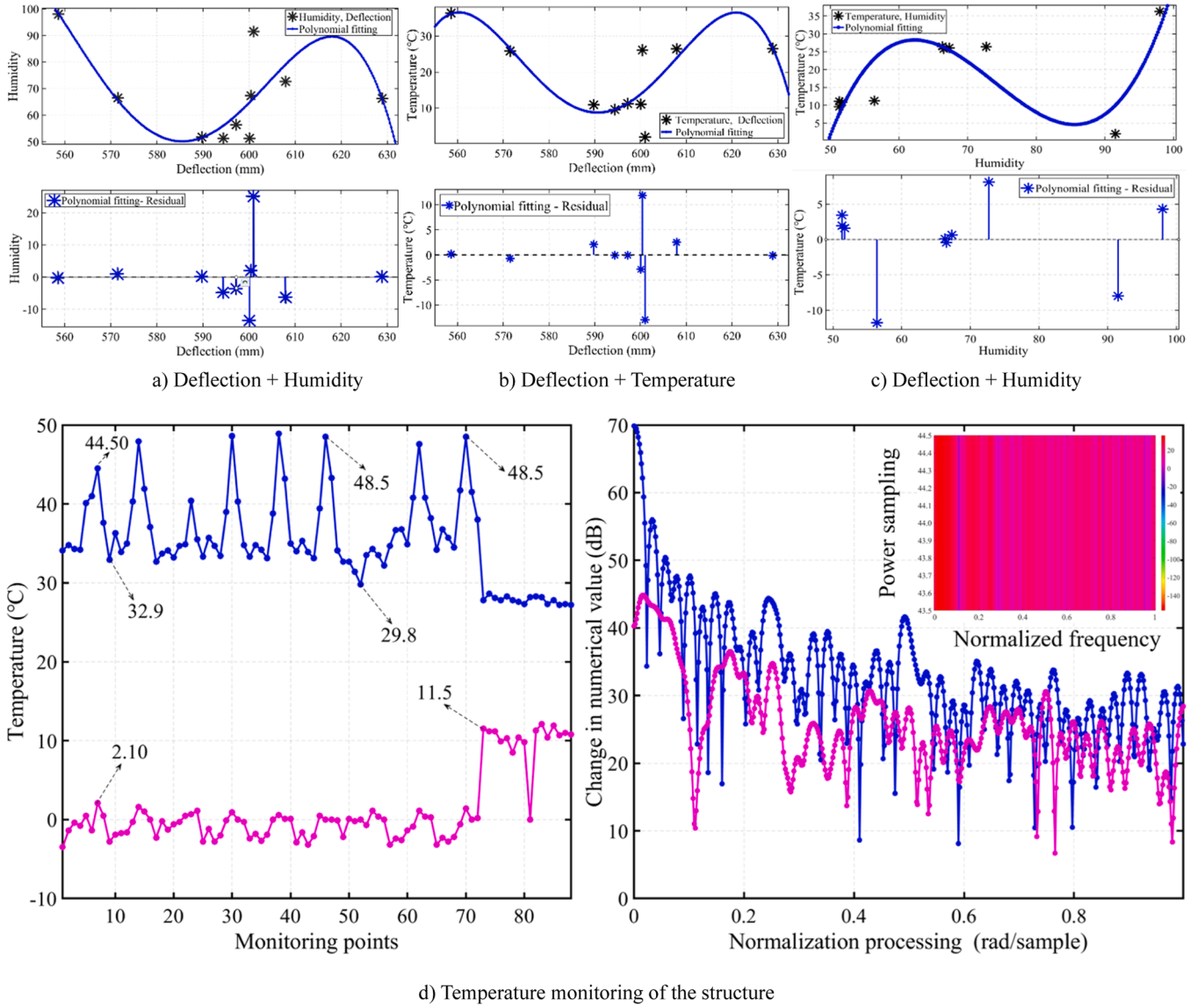
a) Deflection + Humidity   b) Deflection + Temperature   c) Deflection + Humidity

d) Temperature monitoring of the structure

Fig. 9. Linear regression model analysis of the monitoring parameters.

of 7L/12 main beam base plate) $> E_{42403} = 50{,}893.78$ J (right side of 8L/12 main base plate) $> E_{4408} = 37{,}957.27$ J (middle of 7L/12 main beam base plate) $> E_{58696} = 37{,}401.74$ J (10L/12, No. 3 main tower pier column) $> E_{9868} = 36{,}445.67$ J (5L/24, left side of main beam base plate) $> E_{9937} = 31{,}363.68$ J (9L/12, left main beam base plate of No. 3 pier column) $> E_{42358} = 30{,}685.96$ J (4L/12 main beam base plate) $> E_{32714} = 23{,}846.85$ J (middle of 7L/12 main beam top plate) $> E_{32416} = 21{,}486.46$ J (4L/12, right main beam top plate of No. 2 main tower) $> E_{45547} = 20{,}343.44$ J (1L/12, No. 1 main beam base plate) (Fig. 11a). The comprehensive data show that the maximum energy is concentrated in the main beam base plate in ② - ③ spans (marked in orange in Fig. 10a).

The top ten sets of elements in the Strain arrangement are: $S_{134643} = 0.004{,}813$ µε (middle of stay cable 3-1) $> S_{107368} = 0.004{,}532$ µε (middle of stay cable 2-4) $> S_{152592} = 0.004{,}517$ µε (middle of stay cable 3-3) $> S_{80679} = 0.004{,}514$ µε (middle of stay cable 2-2) $> S_{172680} = 0.004{,}813$ µε (middle of stay cable 3-4 stay) $> S_{93010} = 0.004{,}346$ µε (near the cable tower of stay cable 2-1) $> S_{174369} = 0.004{,}345$ µε (near the cable tower of stay cable 3-4) $> S_{145967} = 0.004{,}341$ µε (near the main tower of stay cable 3-2) $> S_{119318} = 0.004{,}419$ µε (middle of stay cable 2-3) $> S_{118413} = 0.003{,}771$ µε (5L/12 section of stay cable 2-3) (Figs. 10d and 11b).

The ranking of Stress is: $ST_{134643} = 991.175$ MPa (middle of stay cable 3-1) $> ST_{107368} = 933.247$ MPa (middle of stay cable 2-4) $> ST_{152592} = 930.772$ MPa (middle of stay cable 3-3) $> ST_{80679} = 929.703$ MPa (middle of stay cable 2-2) $> ST_{172680} = 906.555$M Pa (middle of stay cable 3-4) $> ST_{174369} = 894.954$ MPa (near the cable tower of stay cable 3-4) $> ST_{145967} = 894.545$ MPa (near the main tower of stay cable 3-2) $> ST_{93010} = 893{,}999$M Pa (near the cable tower of stay cable 2-1) $> ST_{119318} = 864.264$ MPa (middle of stay cable 2-3) $> ST_{118413} = 778.347$ MPa (5L/12 section of stay cable 2-3) (Fig. 11c).

The ranking of Displacement is: $D_{5414} = 2.243{,}4$ m (7L/12 main beam base plate) $> D_{32714} = 2.242{,}5$ m (6L/12 main beam top plate) $> D_{42463} = 2.211{,}1$ m (centre of 6L/12 main beam base plate) $> D_{29451} = 2.177{,}9$ m (5L/12 main beam top plate) $> D_{29424} = 2.120{,}8$ m (7L/12 main beam top plate) $> D_{31631} = 2.116{,}4$ m (7L/12 main beam top plate) $> D_{42403} = 2.106{,}3$ m (5L/12 main beam top plate) $> D_{31282} = 2.040{,}2$ m (7L/12 main beam left flange plate) $> D_{31337} = 1.957{,}7$ m (5L/12 main beam base plate) $> D_{63509} = 1.901{,}8$ m (right side of 5L/12 main beam top plate) (Figs. 10d and 11d).

3.2.2. 3D spatial deformation analysis

According to the stress data analysis, the maximum stress is concentrated on the top and base plates of the main beam and so tools were used to analyse the changes in the top and base plates of the main
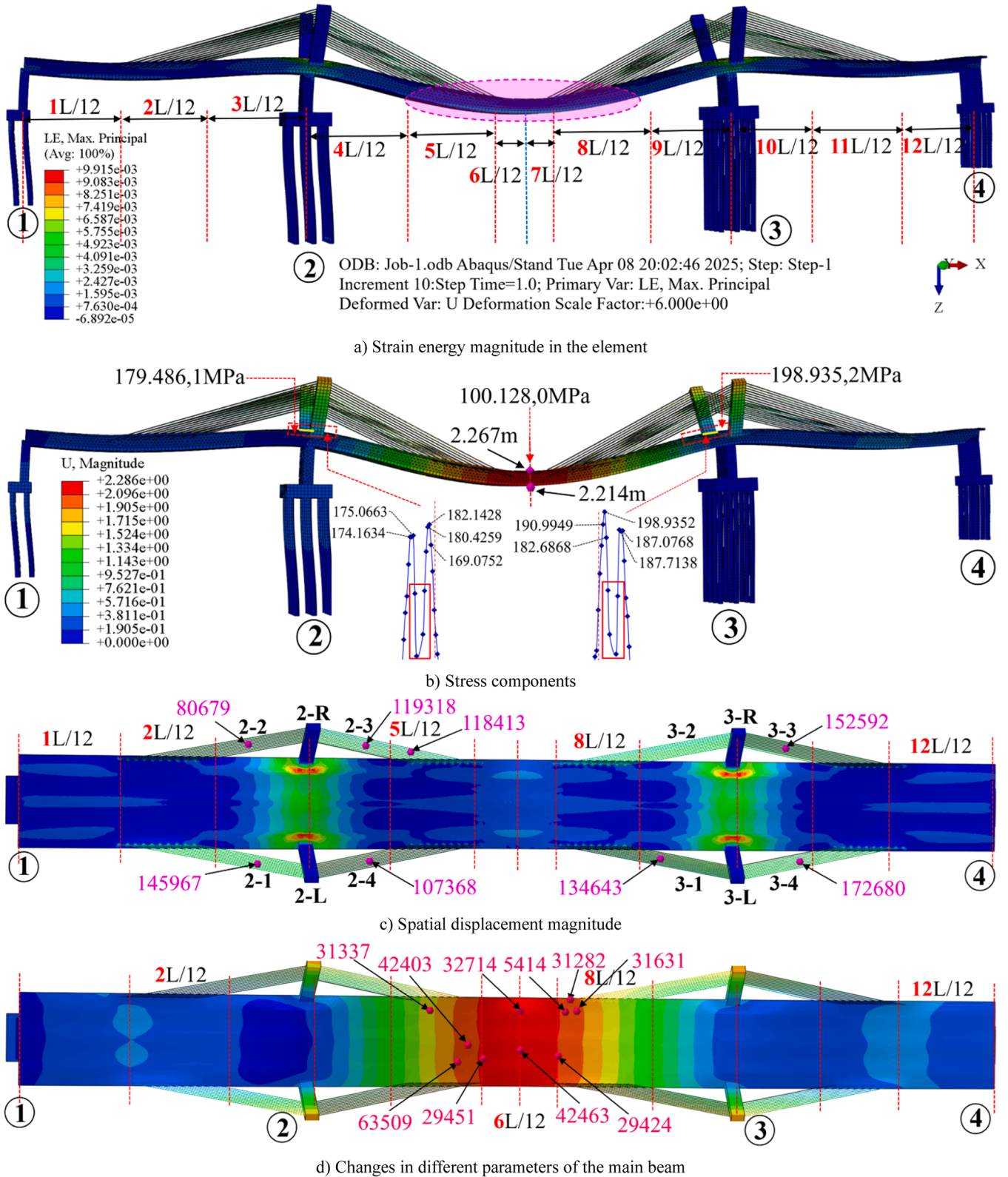
a) Strain energy magnitude in the element

b) Stress components

c) Spatial displacement magnitude

d) Changes in different parameters of the main beam

Fig. 10. LZYB finite element coupling cloud map.

beam. A total of 298 × 4 sets of displacement and stress data were extracted from four positions on both sides of the top and base plates of the main beam, for comparative analysis. This showed that the maximum displacement is $d_{max} = 2.267$ m (middle of 6L/12 main beam, Figs. 12a and 12b), and the minimum displacement is at the hinge position between the main towers ② - ③ and the main beam, i.e. $d_{min} =$ 0.158 m.

The entire displacement curve consists of a concave quadratic parabolic curve, a convex quadratic parabolic curve, and a concave quadratic parabolic curve. The transformation of the main beam base plate curve is consistent with that of the top plate (Fig. 12a). $S_{max} =$ 198.94 MPa and it is concentrated at the hinge position between the
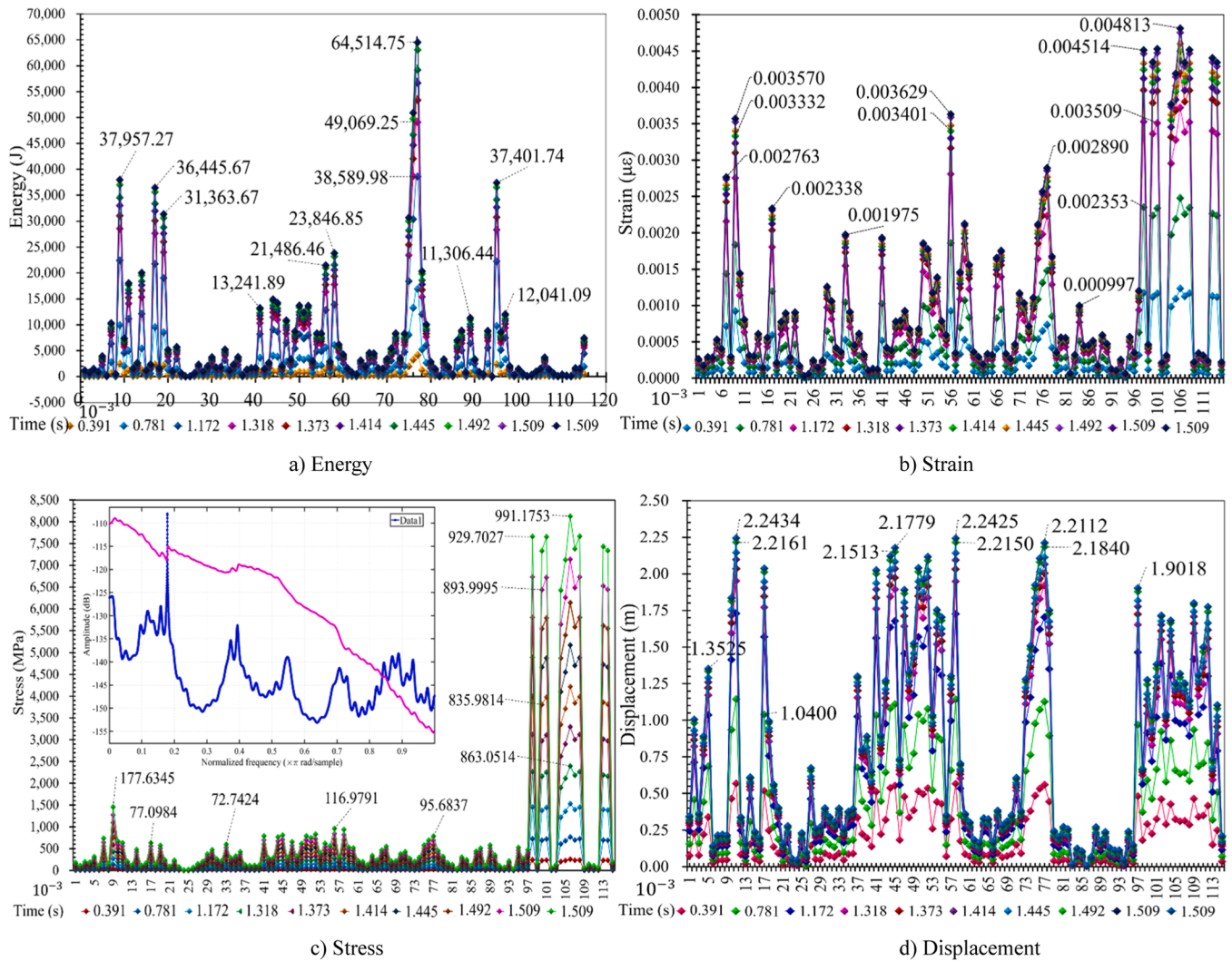
a) Energy

b) Strain

c) Stress

d) Displacement

Fig. 11. LZYB finite element coupling data.

main tower ③ and the main beam. $S_{150m} = 100.128 \sim 101.920$ MPa on the ③ - ② spans and is 50.32% of the main beam ③ (Figs. 10b, 11c, and 11d). The No.

10 cable-stayed cable of the No. 2 and No. 3 main towers is subjected to the greatest stress, with the maximum stress concentrated on the eight cable-stayed cables connecting the tops of the main towers. The stress in the middle area of the cable-stayed cables tends to be stable and the stress increases in the area close to the main beam but is lower than the top area of the main towers (Figs. 12e and 12f).

The stress distribution data of the main towers 2 L, 2R, 3 L, and 3R were collected, obtaining 19 sets of data for each tower. The maximum stress at the consolidation position of the tower pier is $S_{3L-2} = 145.125,7$ MPa > $S_{3R-2} = 136.824,8$ MPa > $S_{2R-1} = 135.212,5$ MPa > $S_{2L-4} = 109.931,9$ MPa and the minimum stress at the top of the tower is $S_{2R-1} = 5.564,0$ MPa (Fig. 10c, 12c, and 12d). The spatial deformation characteristics of two tower columns were analysed using the 3D nonlinear finite element method. The displacements of tower columns 2R and 3 L, at the base of the tower in the x-axis direction, are $-0.040,0 \sim 0.561,9$ m, and the displacement at the top of the tower is $0.244,3 \sim 1.812,3$ m; the displacement at the base of the tower in the y-axis direction is $0.003 \sim 0.088$ m, and the displacement at the top of the tower is $1.631,6 \sim 1.647,1$ m; displacement at the base of the tower in the z-axis direction is $0.301,0 \sim 0.517,5$ m, and the displacement at the top of the tower is $0.394,0 \sim 0.598,6$ m (Fig. 13).

4. Discussion

Using the monitoring data and the finite element coupling analysis in Sections 3.1 and 3.2, a comparison was carried out on the overly conservative design of LYZB under the design load. A sustainable optimised design was created, based on the actual operational characteristics of the project, while taking into account the safety and durability of the structure.

4.1. Stress and displacement coupling analysis

The optimisation of the dynamic characteristics was carried out during on-site monitoring and finite element coupling analysis; a total of 13 sets of maximum stress data were selected for comparative analysis, all within the on-site monitoring range. A polynomial was applied, to carry out the curve fitting analysis, and three indicators were normalised according to mean standardisation, obtaining: $f(x_1) = -153.609,1 \times x^6 - 575.338,4 \times x^5 - 278.701,2 \times x^4 + 1,692.7 \times x^3 - 403.383,0 \times x^2 - 946.157,5 \times x + 990.926,4$; $R^2 = 0.621,5$ (interval mean and main bridge stress). $f(x_2) = 15.595,8 \times x^7 + 6.171,2 \times x^6 - 74.705,4 \times x^5 - 0.745,3 \times x^4 + 96.768,7 \times x^3 - 11.775,7 \times x^2 - 35.604,5 \times x + 189.637,2$; $R^2 = 0.669,2$ (interval mean and main beam stress). Based on the obtained goodness of fit and variance, it can be determined that both indicators meet the interval requirements and the maximum stress only accounts for 0.014% of the interval, indicating a redundant structure.
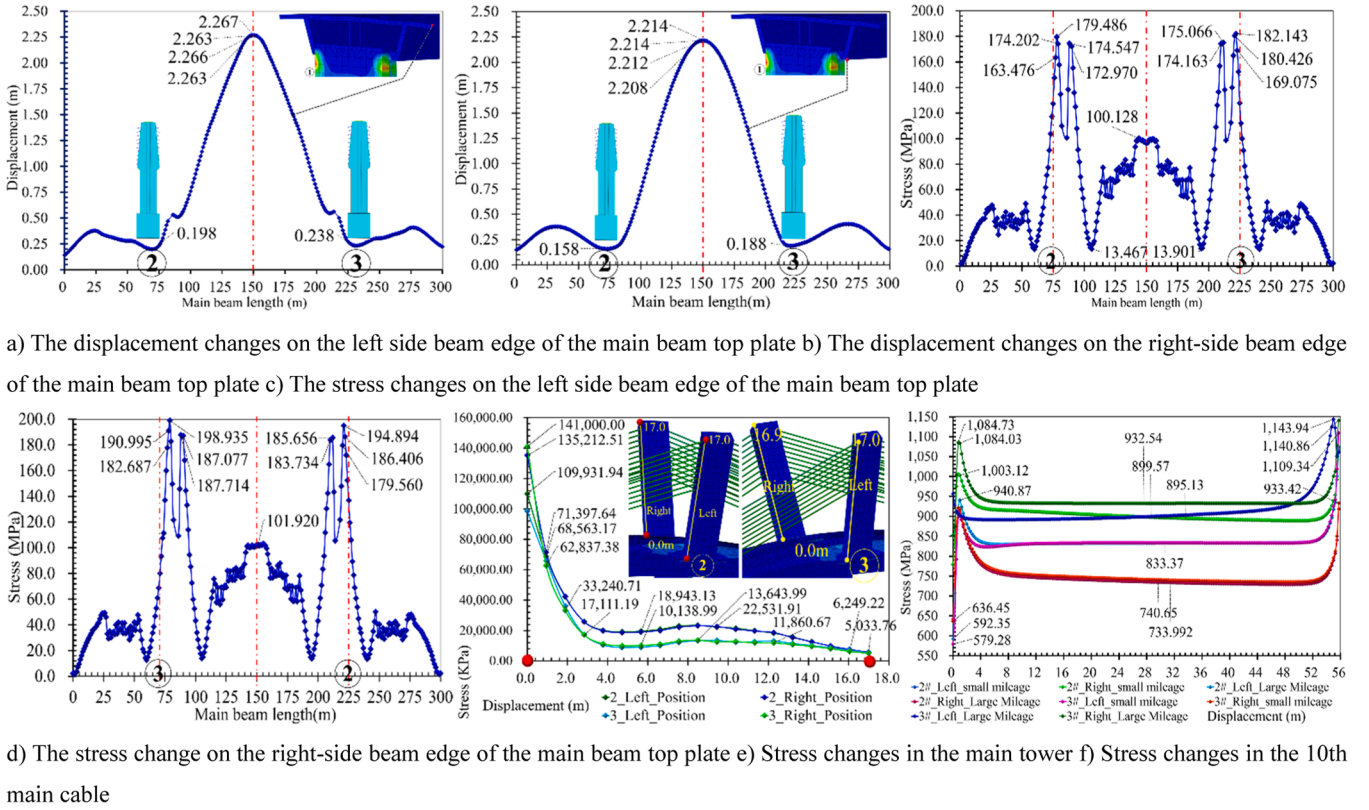
a) The displacement changes on the left side beam edge of the main beam top plate b) The displacement changes on the right-side beam edge of the main beam top plate c) The stress changes on the left side beam edge of the main beam top plate

d) The stress change on the right-side beam edge of the main beam top plate e) Stress changes in the main tower f) Stress changes in the 10th main cable

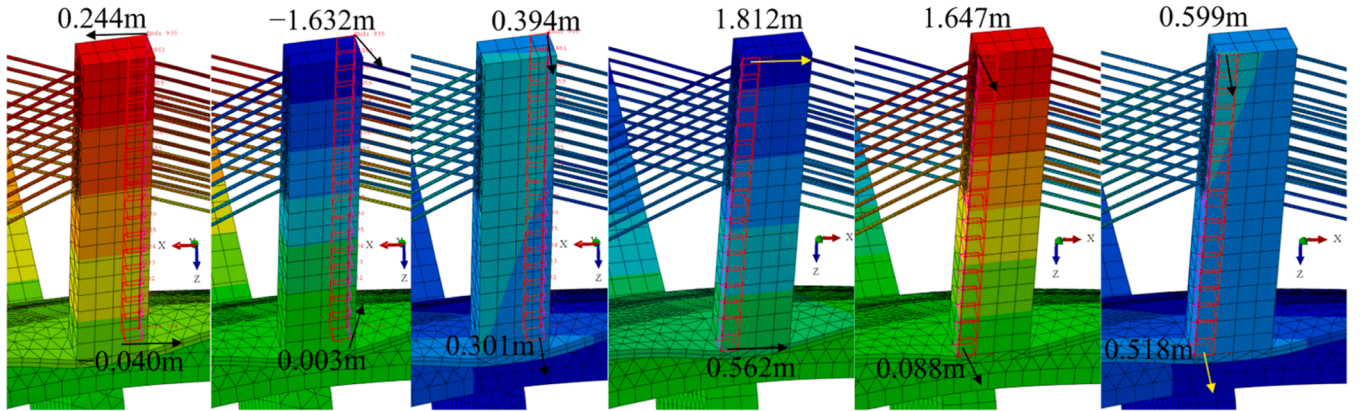**Fig. 12.** LZYB finite element coupling data.

Fig. 13. Three-dimensional deformation analysis of the main tower.

The preliminary conclusion is that local coupling optimisation analysis can be conducted on the main beam. R^2 is the confidence interval for the deflection of the entire bridge, obtained through finite element coupling analysis under the normal operating limit, and is 0.005,9 m $< D_{s1} <$ 2.243,4 m. D_{s1} of the main tower is 0.301,4 m $< D_{s2} <$ 1.678,8 m; D_{s2} is the monitoring deflection range and is 0.002,1 m $< D_{s3} <$ 0.594,4 m. According to the comparative analysis, the overall vertical deflection of LYZB (under multiple loads during its operation) only reaches the design prediction value of 26.50~33.90%. The results of the analysis are consistent with the stress fitting result (Table 4).

4.2. Optimisation analysis of main beam coupling

In accordance with the conclusions of the analysis in Sections 3.1, 3.2, and 4.1 (Eq. (14)), coupling optimisation design was then carried out for the main beam. The change in confidence interval after reducing

the volume of the main beam by $0.1V$ was analysed according to Eq. (15) and the sensitivity impact factor $f_{0.9}$ after each iteration. The optimisation can be represented by a matrix determinant $f_{0.9}^{nm} =$

$$\begin{bmatrix} d_{0.9}^{11} & \cdots & d_{0.9}^{1m} \\ \vdots & \ddots & \vdots \\ d_{0.9}^{n1} & \cdots & d_{0.9}^{nm} \end{bmatrix}, \; A_{0.9}' = f_{0.9} \times A_{0.9} = \begin{bmatrix} 0.5519 \\ \vdots \\ 0.2875 \end{bmatrix} \times \begin{bmatrix} 3724221440 \\ \vdots \\ 3980236032 \end{bmatrix}$$

$$= \begin{bmatrix} 2055459635 \\ \vdots \\ 2196758338 \end{bmatrix}.$$ The parameter index before optimization is $A_{0.9}' =$

$[70, 244, 857.42 \; 78, 471, 844.42 \cdots 1, 340, 564, 588]^T$, $f_{0.9} = [0.0161$ 0.0513 $\cdots 2.5775]$ (Fig. 14b).

Through comparison, it is determined that: $A_{1.0}'$ $=[120, 767, 516.6 \; 240, 250, 634.2 \cdots 2, 353, 562, 136]^T$, $f_{1.0} = [0.0446$ 0.0528 $\cdots 2.2434]$ (Fig. 14a). $A_{0.9}' < A_{1.0}' f_{0.9} > f_{1.0}$, so there is still a

Table 4
Comparison of stress monitoring and finite element data coupling in LZYB.

Monitoring data (1000 GPa)		Finite Element Data (MPa)			
Location number	Stress range	Location number	Full bridge	Location number	Main beam
2.50 spans on the east side	$19.524 > S > -6.725\,S$	32416	116.979,1	78.01	190.994,9
3.50 spans on the east side	$14.613 > S > -6.708\,S$	58696	64.606,5	79.01	198.935,1
3.50 spans on the west side	$18.564 > S > -7.171\,S$	63509	56.926,7	80.02	182.686,8
3.50 spans on the east side	$15.072 > S > -6.295\,S$	80679	929.702,7	88.01	187.713,8
4.25 spans on the west side	$14.998 > > -8.567\,S$	93010	893.999,5	89.01	186.739,8
4.25 spans on the east side	$17.591 > > -6.883\,S$	107368	933.246,5	90.01	187.076,8
4.50 spans on the east side	$17.562 > > -6.382\,S$	118413	778.346,8	91.01	168.019,6
4.75 spans on the west side	$19.822 > > -7.258\,S$	119318	864.263,7	209.87	183.733,8
4.75 spans on the east side	$17.487 > > -7.203\,S$	134643	991.175,3	210.88	184.196,8
5.50 spans on the west side	$18.234 > > -6.828\,S$	145967	896.254,9	211.90	185.655,6
5.50 spans on the east side	$15.632 > > -7.064\,S$	152592	930.771,6	219.91	179.560,1
6.50 spans on the west side	$16.104 > > -6.337\,S$	172680	906.555,4	220.92	194.894,5
6.50 spans on the east side	$17.051 > > -6.628\,S$	174369	894.953,9	221.92	186.405,6

redundant structure after reduction of $0.1V$, and further optimization can be carried out.

The secondary coupling optimization is completed in eight cycles and reduced to $0.85V$. A total of 40 sets of elements are selected for the optimization model to calculate $A'_{0.85} = [73, 463.36\ 73, 599.80 \cdots 240, 529, 174.60]^T$, $f_{0.85} = [0.0131\ 0.0162 \cdots 1.3910]$ (Fig. 14c). Through comparison, it is determined that: $A'_{0.85} < A'_{1.0}, f_{0.85} < f_{1.0}$.

The conclusion which can be drawn from the coupling optimization is that the main beam of LZYB can reduce the amount of concrete by 15%

and that the coupling optimisation area is in the main beam base plate. The main beam is divided into a top plate, flange plate, rib plate, and base plate, all of which are made of C50 reinforced concrete [47–48]. The mechanical equivalent model analysis shows that the top plate transfers the load longitudinally to the base plate, then to the supports and lower structure. The upper and lower plates bear the bending moment and deflection, and the equivalent plate stiffness coefficient is $D_s = E_p \times h_p^3\ /\ 12(1-\mu_p^2)$. The bending moment it bears is $D_r = E_f \times (h+t_0)^2 t_0 /\ 2\ (1-\mu_f^2)$, because the two are equivalent, and $\mu_f = \mu_p, E_p = E_f, h_p = \sqrt[3]{6(h+t_0)^2 t_0}$. According to the analysis of the model data above, the thickness of the base plate has been reduced to 70 mm.

The finite element coupling model of the base plate after reduction is re-established to analyze the dynamic response and plastic effect parameters under the design loads, $A'_{85\%} = [199, 546.24\ 327, 969.38 \cdots 13, 596, 370.68]^T$, $f_{85\%} = [0.001, 1\ 0.003, 2 \cdots 1.601, 7]$ (Fig. 14d), $A'_{85\%} < A'_{1.0}, f_{85\%} < f_{1.0}$. The comparative analysis of data shows that the optimized main beam base plate meets the various load performance requirements of the original design, and its results have important engineering practicality and robustness.

4.3. Sustainable assessment of main beam

A large amount of energy-intensive fossil materials is used in the construction process of statically indeterminate structures but it is difficult to achieve the coupling optimisation of large volumes due to the special design aesthetics and high-performance requirements of such structures. There is a significant spatial spillover effect of structural carbon emissions. Based on the assessment system standards of SDGs 7 & 13 and ISO14040 [49], this study explores the LZYB carbon reduction volume and economic reduction indicators [50–51].

The life cycle assessment (LCA) of LZYB was mainly carried out in the design optimisation stage. The five core indicators selected were: Global warming (GWP100a), AP- Acidification, FEP- Eutrophication, PMFP, and W. The assessment software used was OpenLCA and the database was Ecoinvent, Bedec, and Soca [52–54]. Table 5 shows a reduction of 2, 009.65 tons of CO_2 emissions, 8.86 tons of SO_2 emissions, 7.12 tons of PO4 emissions, and 79.63 tons of other smoke, dust, and waste. The life cycle cost of optimised materials mainly includes the initial material cost, without considering the material maintenance cost and operational costs, and is directly calculated by applying the local project budget estimate quota of the region where LZYB is located, which saves 2,694, 189.55 CNY (Table 5).

Through the comprehensive analysis process described above, we determined that intelligent cloud-based monitoring is the optimal solution for effectively improving maintenance planning requirements and bridge operation and maintenance status data, maximising bridge performance and more economically allocating limited financial budgets to
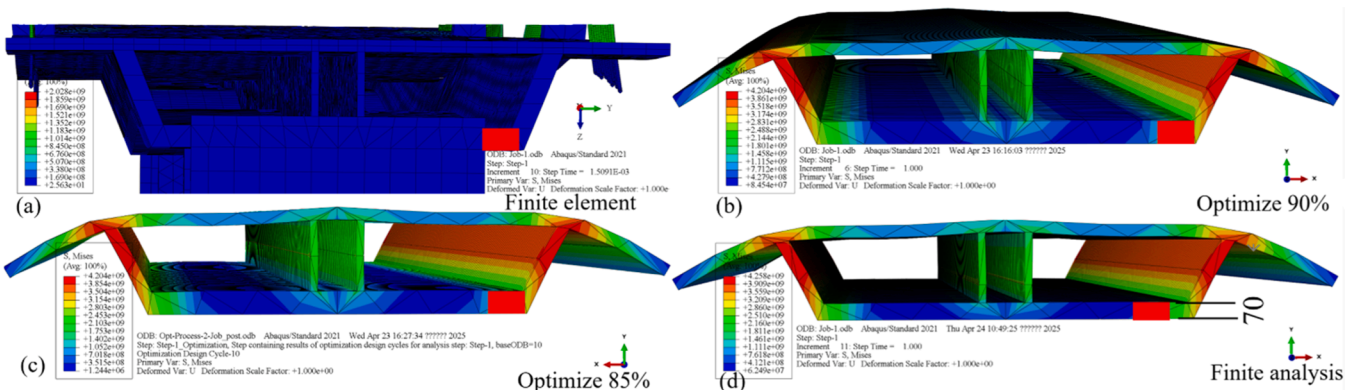
Fig. 14. Finite element analysis and coupling optimisation of the main beam.

Table 5

LCA data evaluation of the optimised main beam of LZYB.

Main beam	Original design	New design	Global warming (GWP100a)	AP- Acidification	FEP- Eutrophication	PMFP	W	Comprehensive price
Material	Quantity (or tone) m^3		Kg					Chinese Yuan: CNY
C50	7,391.90	1,108.79	1,153,141.60	310.46	1,785.15	2,483.69	3.80	1,532,215.83
C40	136.00	20.40	18,768.00	5.10	29.17	41.21	0.07	25,459.57
Steel bar	1,235.60	185.34	837,736.80	8,544.17	5,300.72	29,283.72	47,817.72	1,136,514.15

long-term, efficient bridge maintenance and reducing environmental impact. Over time, through the high-precision prediction of structural damage from non-stationary and nonlinear time degradation sequences, health index measurement and management system integration are achieved.

5. Conclusions

At present, statically indeterminate structures form a significant portion of infrastructure construction and their appearance, construction, and practicality have been favoured by designers. However, they pose difficulties for normal maintenance activities due to the series of consolidation system characteristics which are inherent in their structure. The way to establish a complete and scientific automated early warning and monitoring system, to reduce the large amount of human and financial resources required for maintenance, is a difficult issue that needs to be solved in this field.

The key points and challenges of this research are as follows:

- An innovative, comprehensive assessment model was developed for complex structural systems, addressing the interference of uncertain influencing factors such as natural environmental conditions, uncertain dynamic loads, and structural material degradation.
- A thorough comparative study and analysis were conducted on the theoretical framework, including real-time data monitoring and finite element modelling of hyperstatic structures within an established IoT-based intelligent automated monitoring and early warning cloud platform, demonstrating the platform's effectiveness and advancement.
- The reliability of the monitoring data was validated through research involving a three-dimensional dynamic hyperstatic model, leading to a rational optimisation design and evaluation aimed at the sustainable development of hyperstatic structures.
- Research findings and scientific perspectives on the real-time monitoring scheme were proposed, to serve as references for design units and management departments.

The key findings of this research are:

- Cable failure is a critical factor affecting the stability and normal operation of cable-stayed bridges; it is a primary target for monitoring. Typically, stress or displacement fibre optic monitoring equipment is installed at intervals between the tower sections; however, this arrangement is suboptimal.
- Analysis of the cable surface stress on a twin-tower cable-stayed bridge shows that the highest cable stress is concentrated on the longest cable, cable No. 10, with the maximum stress occurring within 2 m of the main tower top.
- Stress in the central region of the cable plane (2–52 m) remains essentially stable, allowing for a limited number of monitoring points to be installed in the intermediate sections.
- Stress in the area surrounding the connection between the cable and the main beam (up to 3 m) increases rapidly, forming a peak at the turning point. The stress ratios in the three regions are 1.072, 1.000, and 1.066. The current layout of intelligent cable force monitoring points is inadequate: no monitoring points are installed at the tower top, while too many are placed at the main beam, resulting in inefficient use of the equipment.
- Analysis of the monitoring data reveals that internal forces in other components within the same area are essentially consistent. Therefore, the routine maintenance of cable-stayed cables should focus on the connection between the tower top and the main beam.

The innovation of this article lies in the systematic application of measured data and 3D finite element modelling to analyse the safety and coupling optimisation problems of super-large bridges during their operation under multiple influencing factors, providing an example for real-time monitoring of intelligent cloud platforms and comparative analysis of the data robustness of similar statically indeterminate structures. This results in overcoming the drawbacks of traditional daily maintenance that requires a large amount of human and financial resources. There are still shortcomings in the study, such as the insufficient in-depth study on the mechanism of destructive effects of overloading, overweight and overspeed, etc. Subsequent in-depth research in this direction should be carried out whilst operating under continuous monitoring and early warning systems.

Data availability

Data will be made available on request.

CRediT authorship contribution statement

Zhiwu Zhou: Writing – review & editing, Writing – original draft, Software, Methodology, Investigation, Funding acquisition, Formal analysis, Data curation, Conceptualization. **Zhifeng Zhao:** Visualization, Validation, Software, Resources, Formal analysis, Data curation. **Julián Alcalá:** Supervision, Resources, Project administration, Methodology, Formal analysis, Data curation, Conceptualization. **Víctor Yepes:** Visualization, Validation, Supervision, Project administration, Investigation, Funding acquisition, Formal analysis.

Declaration of competing interest

The authors declare that they have no known competing financial interests or personal relationships that could have appeared to influence the work reported in this paper.

Funding sources

References

[1] S. Karimi, O. Mirza, Damage identification in bridge structures: review of available methods and case studies, Aust. J. Struct. Eng. 24 (2023) 89–119, https://doi.org/10.1080/13287982.2022.2120239.

[2] B.T. Svendsen, G.T. Frøseth, O. Øiseth, A. Rønnquist, A data-based structural health monitoring approach for damage detection in steel bridges using experimental data, J. Civ. Struct. Health Monit. 12 (2022) 101–115, https://doi.org/10.1007/s13349-021-00530-8.

[3] X. Han, D.M. Frangopol, Fatigue reliability analysis considering corrosion effects and integrating SHM information, Eng. Struct. 272 (2022) 114967, https://doi.org/10.1016/j.engstruct.2022.114967.

[4] R.R. Rabi, M. Vailati, G. Monti, Effectiveness of vibration-based techniques for damage localization and lifetime prediction in structural health monitoring of bridges: a comprehensive review, Buildings 14 (2024) 1183, https://doi.org/10.3390/buildings14041183.

[5] Q. Wei, B. Kövesdi, L. Dunai, M. Cao, Formulation of dynamic damage features sensitive to local fatigue cracks in steel bridges: numerical study, Structures 67 (2024) 107049, https://doi.org/10.1016/j.istruc.2024.107049.

[6] S. Yu, J. Ou, Fatigue life prediction for orthotropic steel deck details with a nonlinear accumulative damage model under pavement temperature and traffic loading, Eng. Fail. Anal. 126 (2021) 105366, https://doi.org/10.1016/j.engfailanal.2021.105366.

[7] A. Alsehaimi, M. Houda, A. Waqar, S. Hayat, F. Ahmed Waris, O. Benjeddou, Internet of things (IoT) driven structural health monitoring for enhanced seismic resilience: a rigorous functional analysis and implementation framework, Results Eng. 22 (2024) 102340, https://doi.org/10.1016/j.rineng.2024.102340.

[8] M. Aqeel, M.A. Nasir, Z.U. Rehman, S. Nauman, A. Wakeel, E.G. Hanna, Development of AgNPs-PVP/TPU based flexible strain sensors for structural health monitoring of composite structures, Results Eng. 23 (2024) 102526, https://doi.org/10.1016/j.rineng.2024.102526.

[9] S.N. Pakzad, G.L. Fenves, S. Kim, D.E. Culler, Design and implementation of scalable wireless sensor network for structural monitoring, J. Infrastruct. Syst. 14 (2008) 89–101, https://doi.org/10.1061/(ASCE)1076-0342(2008)14:1(89).

[10] S.A. Taher, J. Li, J.-H. Jeong, S. Laflamme, H. Jo, C. Bennett, W.N. Collins, A.R. J. Downey, Structural health monitoring of fatigue cracks for steel bridges with wireless large-area strain sensors, Sensors 22 (2022) 5076, https://doi.org/10.3390/s22145076.

[11] Y. Lai, Smart city space simulation based on multidimensional sensing networks and green energy intelligent decision support, Results Eng. 27 (2025) 105674, https://doi.org/10.1016/j.rineng.2025.105674.

[12] K. Kumar, P.K. Biswas, N. Dhang, Time series-based SHM using PCA with application to ASCE benchmark structure, J. Civ. Struct. Health Monit. 10 (2020) 899–911, https://doi.org/10.1007/s13349-020-00423-2.

[13] G. Galanopoulos, D. Milanoski, N. Eleftheroglou, A. Broer, D. Zarouchas, T. Loutas, Acoustic emission-based remaining useful life prognosis of aeronautical structures subjected to compressive fatigue loading, Eng. Struct. 290 (2023) 116391, https://doi.org/10.1016/j.engstruct.2023.116391.

[14] J.-A. Li, D. Feng, Fatigue life evaluation of bridge stay cables subject to monitoring traffic and considering road roughness, Eng. Struct. 293 (2023) 116572, https://doi.org/10.1016/j.engstruct.2023.116572.

[15] Study on bridge structure damage and health diagnosis method based on health monitoring, Tehnicki Vjesnik - Technical Gazette 28 (2021). https://doi.org/10.17559/TV-20200522094215.

[16] A. Sofi, J.Jane Regita, B. Rane, H.H. Lau, Structural health monitoring using wireless smart sensor network – an overview, Mech. Syst. Signal Process. 163 (2022) 108113, https://doi.org/10.1016/j.ymssp.2021.108113.

[17] B. Yong, G. Zhang, H. Chen, Q. Zhou, Intelligent monitor system based on cloud and convolutional neural networks, J. Supercomput. 73 (2017) 3260–3276, https://doi.org/10.1007/s11227-016-1934-1.

[18] Y. Luo, H. Zheng, H. Zhang, Y. Liu, Fatigue reliability evaluation of aging prestressed concrete bridge accounting for stochastic traffic loading and resistance degradation, Adv. Struct. Eng. 24 (2021) 3021–3029, https://doi.org/10.1177/13694332211017995.

[19] G.-R. Gillich, H. Furdui, M. Abdel Wahab, Z.-I. Korka, A robust damage detection method based on multi-modal analysis in variable temperature conditions, Mech. Syst. Signal Process. 115 (2019) 361–379, https://doi.org/10.1016/j.ymssp.2018.05.037.

[20] S. Mustafa, Y. Matsumoto, H. Yamaguchi, Vibration-based health monitoring of an existing truss bridge using energy-based damping evaluation, J. Bridge Eng. 23 (2018), https://doi.org/10.1061/(ASCE)BE.1943-5592.0001159.

[21] J. Shen, Z. Li, S. Luo, W. Wang, A structural damage identification method based on arrangement of the static force residual vector, Front. Mater. 9 (2022), https://doi.org/10.3389/fmats.2022.918069.

[22] Q.W. Yang, J.K. Liu, Structural damage identification based on residual force vector, J. Sound Vib. 305 (2007) 298–307, https://doi.org/10.1016/j.jsv.2007.03.033.

[23] Z. Waszczyszyn, L. Ziemiański, Neural networks in mechanics of structures and materials – new results and prospects of applications, Comput. Struct. 79 (2001) 2261–2276, https://doi.org/10.1016/S0045-7949(01)00083-9.

[24] F. Mostofi, Ü. Bahadır, O.B. Tokdemir, V. Toğan, V. Yepes, Enhancing strategic investment in construction engineering projects: a novel graph attention network decision-support model, Comput. Ind. Eng. 203 (2025) 111033, https://doi.org/10.1016/j.cie.2025.111033.

[25] A. Zubaydi, M.R. Haddara, A.S.J. Swamidas, Damage identification in a ship's structure using neural networks, Ocean Eng. 29 (2002) 1187–1200, https://doi.org/10.1016/S0029-8018(01)00077-4.

[26] G.E. Hinton, R.R. Salakhutdinov, Reducing the dimensionality of data with neural networks, Science (1979) 313 (2006) 504–507, https://doi.org/10.1126/science.1127647.

[27] K. Worden, G. Manson, N.R.J. Fieller, Damage detection using outlier analysis, J. Sound Vib. 229 (2000) 647–667, https://doi.org/10.1006/jsvi.1999.2514.

[28] J. Spross, T. Gasch, Reliability-based alarm thresholds for structures analysed with the finite element method, Struct. Saf. 76 (2019) 174–183, https://doi.org/10.1016/j.strusafe.2018.09.004.

[29] L.J. Prendergast, D. Hester, Isolating the location of scour-induced stiffness loss in bridges using local modal behaviour, J. Civ. Struct. Health Monit. 7 (2017) 483–503, https://doi.org/10.1007/s13349-017-0238-3.

[30] H.-S. Shang, T.-H. Yi, L.-S. Yang, Experimental study on the compressive strength of big mobility concrete with nondestructive testing method, Adv. Mater. Sci. Eng. 2012 (2012) 1–6, https://doi.org/10.1155/2012/345214.

[31] J.-B. Ihn, F.-K. Chang, Detection and monitoring of hidden fatigue crack growth using a built-in piezoelectric sensor/actuator network: I. Diagnostics, Smart Mater. Struct. 13 (2004) 609–620, https://doi.org/10.1088/0964-1726/13/3/020.

[32] J. Li, K.A. Mechitov, R.E. Kim, B.F. Spencer, Efficient time synchronization for structural health monitoring using wireless smart sensor networks, Struct. Control Health Monit. 23 (2016) 470–486, https://doi.org/10.1002/stc.1782.

[33] C. Zou, Z. Ibrahim, H. Hashim, A. Jamadin, P. Ayough, Nonlinear analysis of reinforced concrete slabs under high-cyclic fatigue loading, J. Mater. Res. Technol. 21 (2022) 992–1012, https://doi.org/10.1016/j.jmrt.2022.09.091.

[34] Z. Lei, L. Zhu, Y. Fang, C. Niu, Y. Zhao, Fiber bragg grating smart material and structural health monitoring system based on digital twin drive, J. Nanomater. (2022) 2022, https://doi.org/10.1155/2022/4356974.

[35] A.R. Al-Ali, S. Beheiry, A. Alnabulsi, S. Obaid, N. Mansoor, N. Odeh, A. Mostafa, An IoT-based road bridge health monitoring and warning system, Sensors 24 (2024) 469, https://doi.org/10.3390/s24020469.

[36] G. Zhang, Y. Liu, J. Liu, S. Lan, J. Yang, Causes and statistical characteristics of bridge failures: a review, J. Traffic Transp. Eng. (Engl. Ed.) 9 (2022) 388–406, https://doi.org/10.1016/j.jtte.2021.12.003.

[37] X. Liu, W. Han, Y. Yuan, X. Chen, Q. Xie, Corrosion fatigue assessment and reliability analysis of short suspender of suspension bridge depending on refined traffic and wind load condition, Eng. Struct. 234 (2021) 111950, https://doi.org/10.1016/j.engstruct.2021.111950.

[38] Y. Ma, H. Zhou, Y. He, X. Li, L. Wang, Subcycle corrosion fatigue crack growth model for bridge suspender wires under random time-series loads, Eng. Fail. Anal. 169 (2025) 109183, https://doi.org/10.1016/j.engfailanal.2024.109183.

[39] P. Rizzo, A. Enshaeian, Challenges in bridge health monitoring: a review, Sensors 21 (2021) 4336, https://doi.org/10.3390/s21134336.

[40] B.T. Svendsen, O. Øiseth, G.T. Frøseth, A. Rønnquist, A hybrid structural health monitoring approach for damage detection in steel bridges under simulated environmental conditions using numerical and experimental data, Struct. Health Monit. 22 (2023) 540–561, https://doi.org/10.1177/14759217221098998.

[41] V. Yepes, C. Torres-machi, A. Chamorro, E. Pellicer, Optimal pavement maintenance programs based on a hybrid greedy randomized adaptive search procedure algorithm, J. Civ. Eng. Manag. 22 (2016) 540–550, https://doi.org/10.3846/13923730.2015.1120770.

[42] D. Anastasopoulos, E.P.B. Reynders, Modal strain monitoring of the old Nieuwebrugstraat bridge: local damage versus temperature effects, Eng. Struct. 296 (2023) 116854, https://doi.org/10.1016/j.engstruct.2023.116854.

[43] P. Vanova, Z. Sun, O.-E. Odinson, Z. Jiang, Dynamic response analysis of a model truss bridge considering damage scenarios, Eng. Fail. Anal. 151 (2023) 107389, https://doi.org/10.1016/j.engfailanal.2023.107389.

[44] H.M.K.D. Wickramathilaka, D. Fernando, D. Jayasundara, D. Wickramasinghe, D.Y.L. Ranasinghe, G.M.R.I. Godaliyadda, M.P.B. Ekanayake, H.M.V.R. Herath, L. Ramanayake, N. Senarath, H.M.H.K. Weerasooriya, GAUSS: guided encoder - decoder architecture for hyperspectral unmixing with spatial smoothness, Eur. J. Remote Sens. 56 (2023), https://doi.org/10.1080/22797254.2023.2277213.

[45] Y.I. Shah, Z. Hu, J. Huang, Study on tension control method of anchor span for three tower suspension bridge, Structures 58 (2023) 105431, https://doi.org/10.1016/j.istruc.2023.105431.

[46] S.-S. Jin, Y.-S. Park, S. Kim, Y.-H. Park, Model updating based on mixed-integer nonlinear programming under model-form uncertainty in finite element model, Eng. Comput. 37 (2021) 3699–3725, https://doi.org/10.1007/s00366-020-01030-x.

[47] J. Garcia, G. Villavicencio, F. Altimiras, B. Crawford, R. Soto, V. Minatogawa, M. Franco, D. Martínez-Muñoz, V. Yepes, Machine learning techniques applied to construction: a hybrid bibliometric analysis of advances and future directions, Autom. Constr. 142 (2022) 104532, https://doi.org/10.1016/j.autcon.2022.104532.

[48] H. Liu, J. Huang, W. Zhang, Numerical algorithm based on extended barycentric Lagrange interpolant for two dimensional integro-differential equations, Appl. Math. Comput. 396 (2021) 125931, https://doi.org/10.1016/j.amc.2020.125931.

[49] P. Wen, K. Ji, R. Wen, Simplified procedure for simulating artificial non-stationary multi-point earthquake accelerograms, Soil Dyn. Earthq. Eng. 156 (2022) 107239, https://doi.org/10.1016/j.soildyn.2022.107239.

[50] R.K. Luo, Creep prediction with temperature effect and experimental verification of rubber suspension components used in rail vehicles, Proc. Inst. Mech. Eng. C J. Mech. Eng. Sci. 233 (2019) 3950–3963, https://doi.org/10.1177/0954406218809143.

[51] X. Ding, X. Mao, X. Yuan, Study on the seismic performance of a new straw ecological composite wall structure, Structures 65 (2024) 106640, https://doi.org/10.1016/j.istruc.2024.106640.

[52] Y. Yang, X. Su, Spatial correlation network structure of carbon emission reduction capacity on urban agglomerations and its driving factors: a perspective of

sustainable development goals, Sustain. Cities Soc. 113 (2024) 105646, https://doi.org/10.1016/j.scs.2024.105646.

[53] Z.W. Zhou, J. Alcalà, V. Yepes, Carbon impact assessment of bridge construction based on resilience theory, J. Civ. Eng. Manag. 29 (2023) 561–576, https://doi.org/10.3846/jcem.2023.19565.

[54] Z. Zhou, J. Zhou, J. Alcalá, V. Yepes, Thermal coupling optimization of bridge environmental impact under natural conditions, Env. Impact Assess. Rev. 104 (2024) 107316, https://doi.org/10.1016/j.eiar.2023.107316.